ATLAS CONF Note

ATLAS-CONF-2019-050

2nd October 2019

Test of CP invariance in vector-boson fusion production of the Higgs boson in the $H \to \tau\tau$ channel in proton–proton collisions at $\sqrt{s} = 13$ TeV with the ATLAS detector

The ATLAS Collaboration

A test of CP invariance in Higgs boson production via vector-boson fusion in the $H \to \tau\tau$ decay mode is presented. This test uses the Optimal Observable method and is carried out using 36.1 fb^{-1} of $\sqrt{s} = 13$ TeV proton–proton collision data collected by the ATLAS experiment at the LHC. Contributions from CP-violating interactions between the Higgs boson and electroweak gauge bosons are described by an effective field theory, in which the parameter $\tilde{d}$ governs the strength of CP violation. No sign of CP violation is observed in the distributions of the Optimal Observable, and $\tilde{d}$ is constrained to the interval $[-0.090, 0.035]$ at the 68% confidence level (CL), compared to an expected interval of $\tilde{d} \in [-0.035, 0.033]$ based upon the Standard Model prediction. No constraints can be set on $\tilde{d}$ at 95% CL, while an expected 95% CL interval of $\tilde{d} \in [-0.21, 0.15]$ for the Standard Model hypothesis was expected.

ATLAS-CONF-2019-050
17 October 2019

© 2019 CERN for the benefit of the ATLAS Collaboration.
Reproduction of this article or parts of it is allowed as specified in the CC-BY-4.0 license.

Contents

1 Introduction 2

2 Theoretical framework and methodology 3

3 ATLAS detector 6

4 Simulated event samples 6

5 Event selection 8

6 Background estimation 11

7 Systematic uncertainties 13

8 Fitting procedure 14

9 Results 15

10 Conclusion 20

Appendix 21

1 Introduction

One of the central open puzzles in physics today is the explanation of the observed baryon asymmetry of the universe. The violation of invariance of fundamental interactions under the transformation of charge conjugation (C) and its combination with parity (CP) is one of the three necessary Sakharov conditions [1] to explain the dynamical generation of the baryon asymmetry. In the Standard Model (SM) of particle physics, CP violation (CPV) is introduced via the complex phase in the quark mixing (CKM) matrix [2, 3][1]. It is able to describe all observations of CPV in the K-, B-, and D-meson systems [4–13].

However, the measured size of the complex phase and the derived magnitude of CP violation in the early universe is insufficient to explain the observed value of the baryon asymmetry within the SM [14–18] and, most probably, new sources of CPV beyond the SM need to be introduced.

The investigation of Higgs boson production and decay at the LHC offers a novel opportunity to search for new sources of CPV in the interaction of the Higgs boson with other SM particles. No observable effect of CPV is expected in the production or decay of the SM Higgs boson. Hence any observation of CP violation involving the observed Higgs boson [19, 20] would be an unequivocal sign of physics beyond the SM.

The measured Higgs boson production cross sections, branching ratios, and derived constraints on coupling-strength modifiers, assuming the tensor structure of the SM, agree with the SM predictions within the current precision [21–23]. Investigations of spin and CP quantum numbers strongly indicate that the observed particle is of scalar nature, and that the dominant coupling structure is CP-even and consistent

[1] Effects of possible CPV in the neutrino sector and in the strong interaction are not considered in this statement.

with the SM expectation [24–26]. Limits on Wilson coefficients in the framework of effective field theories multiplying CP-even and CP-odd operators, which modify the coupling structure and strength of the Higgs boson to gluons and electroweak gauge bosons have been derived from various measurements. These include measurements of differential cross-sections of CP-even observables in the decay $H \to \gamma\gamma$ [27], measurements of event rates in specific event categories and phase space regions in the decay $H \to ZZ$ [28], and measurements of the VH invariant mass in Higgs-boson production in association with a weak gauge boson V ($V = W^{\pm}, Z$) [29]. These analyses use CP-even observables and event rate information and hence are not directly sensitive to possible interference between the CP-even SM operators and new CP-odd operators. The shape of distributions of CP-odd and CP-even observables (without exploiting CP-even rate information) have been used to set limits on couplings multiplying CP-odd and CP-even operators of the Higgs boson to gauge bosons by investigating the decay $H \to VV (V = W^{\pm}, Z)$ using only information from the decay [25, 30] and combining it with information from vector boson fusion (VBF) or associated VH production [31, 32], and by utilizing the decay $H \to \tau\tau$ using information from VBF and VH production [33]. The shape of a single CP-odd observable constructed from kinematic information in VBF production from the decay $H \to \tau\tau$ has been previously used to set a limit on the parameter $\tilde{d}$ [34], which governs the strength of CPV in an effective field theory ansatz as described in Section 2. This analysis constrained $\tilde{d}$ to the interval $[-0.11, 0.05]$ at the 68% CL using ATLAS data collected at $\sqrt{s} = 8$ TeV in 2012, while a 68% CL interval of $\tilde{d} \in [-0.16, 0.16]$ was expected. No hints for CPV have been observed in these studies.

In this paper, a direct test of CP invariance in Higgs boson production via VBF is presented in the $H \to \tau\tau$ channel, based on proton–proton collision data corresponding to an integrated luminosity of 36.1 fb^{-1} collected with the ATLAS detector at $\sqrt{s} = 13$ TeV in the years 2015 and 2016. A CP-odd Optimal Observable [35–37] is employed. The Optimal Observable combines the information from the multi-dimensional phase space in a single quantity calculated from leading-order matrix elements for VBF production, independent of the decay mode of the Higgs boson. VBF production provides a promising physics process to test CP invariance in the HVV vertex [38], and the decay mode $H \to \tau\tau$ allows the selection of signal events with a good signal-to-background ratio and the reconstruction of the four-momentum of the Higgs boson candidate with adequate precision.

In the present work a direct test of CP invariance is possible through a measurement of the mean value of the CP-odd Optimal Observable, neglecting possible effects from rescattering by new light particles in loops [38]. Moreover, a measurement of the parameter $\tilde{d}$ is performed. Limits on $\tilde{d}$ are derived by analyzing the shape of spectra of the Optimal Observable measured in $H \to \tau\tau$ candidate events with two jets in the final state consistent with VBF production. The event selection, estimation of background contributions and systematic uncertainties closely follow the analysis employed for the observation of the $H \to \tau\tau$ decay [39]. In order to increase the signal-to-background ratio, the final event selection utilizes multivariate discriminants.

2 Theoretical framework and methodology

The effective Lagrangian $\mathcal{L}_{\text{eff}}$ considered is the SM Lagrangian augmented with CP-odd operators of mass dimension six, involving the Higgs field and electroweak gauge fields. No CP-even dimension-six operators built from these fields are taken into account. All interactions between the Higgs boson and other SM particles (fermions and gluons) are assumed to be as predicted in the SM, i.e. the coupling structure in gluon–gluon fusion production and in the decay into a pair of τ-leptons is considered to be the same as in

the SM. The theoretical ansatz considered and the methodology is the same as in Ref. [34] which contains further details. After electroweak symmetry breaking, the Lagrangian can be written in the mass basis of the Higgs boson H, photon A and weak gauge bosons $W^{\pm}$ and Z as in Ref. [40]:

$$\mathcal{L}_{\text{eff}} = \mathcal{L}_{\text{SM}} + \tilde{g}_{HAA} H \tilde{A}_{\mu\nu} A^{\mu\nu} + \tilde{g}_{HAZ} H \tilde{A}_{\mu\nu} Z^{\mu\nu} + \tilde{g}_{HZZ} H \tilde{Z}_{\mu\nu} Z^{\mu\nu} + \tilde{g}_{HWW} H \tilde{W}^{+}_{\mu\nu} W^{-\mu\nu} ,$$

where $V^{\mu\nu}$ and $\tilde{V}^{\mu\nu} = \epsilon^{\mu\nu\rho\sigma} V_{\rho\sigma}$ (with $V = W^{\pm}, Z, A$) denote the field strength and dual field strength tensors, respectively. Only two of the four couplings $\tilde{g}_{HVV'}$ are independent due to constraints imposed by $\mathrm{U}(1)_Y$ and $\mathrm{SU}(2)_{I_W,\mathrm{L}}$ invariance. They can be expressed in terms of two dimensionless couplings $\tilde{d}$ and $\tilde{d}_B$ as in Refs. [41, 42]:

$$\tilde{g}_{HAA} = \frac{g}{2m_W}(\tilde{d} \sin^2\theta_W + \tilde{d}_B \cos^2\theta_W) \qquad \tilde{g}_{HAZ} = \frac{g}{2m_W} \sin 2\theta_W (\tilde{d} - \tilde{d}_B)$$
$$\tilde{g}_{HZZ} = \frac{g}{2m_W}(\tilde{d} \cos^2\theta_W + \tilde{d}_B \sin^2\theta_W) \qquad \tilde{g}_{HWW} = \frac{g}{m_W}\tilde{d},$$

where g is the SU(2) coupling constant and θ_W is the weak mixing angle. Adopting the arbitrary choice $\tilde{d} = \tilde{d}_B$ yields the following relations[2]:

$$\tilde{g}_{HAA} = \tilde{g}_{HZZ} = \frac{1}{2}\tilde{g}_{HWW} = \frac{g}{2m_W}\tilde{d} \quad \text{and} \quad \tilde{g}_{HAZ} = 0 .$$

In an effective field theory, the coupling parameters are real valued. However, rescattering effects from new particles in loops, with masses lower than the scale of new physics assumed in the EFT, may introduce an imaginary part [38]. Such effects are not considered in the analysis presented here, as $\tilde{d}$ is assumed to be real valued.

The strength of CP-violation in VBF Higgs boson production is then described by a single parameter $\tilde{d}$. The corresponding matrix element $\mathcal{M}$ for VBF production is the sum of a CP-even contribution $\mathcal{M}_{\text{SM}}$ from the SM and a CP-odd contribution $\mathcal{M}_{\text{CP-odd}}$ from the dimension-six operators considered:

$$\mathcal{M} = \mathcal{M}_{\text{SM}} + \tilde{d} \cdot \mathcal{M}_{\text{CP-odd}},$$

where the dependence on $\tilde{d}$ has explicitly been factorized out. The squared matrix element has three contributions:

$$|\mathcal{M}|^2 = |\mathcal{M}_{\text{SM}}|^2 + \tilde{d} \cdot 2\,\mathrm{Re}(\mathcal{M}^*_{\text{SM}} \mathcal{M}_{\text{CP-odd}}) + \tilde{d}^2 \cdot |\mathcal{M}_{\text{CP-odd}}|^2 .$$

The first term $|\mathcal{M}_{\text{SM}}|^2$ and third term $\tilde{d}^2 \cdot |\mathcal{M}_{\text{CP-odd}}|^2$ are both CP-even and hence are not a source of CPV. The second term $\tilde{d} \cdot 2\,\mathrm{Re}(\mathcal{M}^*_{\text{SM}} \mathcal{M}_{\text{CP-odd}})$ stems from the interference of the two contributions to the matrix element and is CP-odd, representing a possible new source of CPV in the Higgs sector. The interference term integrated over a CP-symmetric part of phase space vanishes and therefore does not contribute to the total cross section and observed event yield after applying CP-symmetric selection criteria. The third term increases the total cross section by an amount quadratic in $\tilde{d}$, but this is not exploited in the analysis presented here as the observed rate can also be influenced by additional CP-conserving new physics.

The final state consisting of the reconstructed decay of the Higgs boson and the two tagging jets corresponding to the VBF topology can be characterized by seven phase-space variables, by fixing the mass of the Higgs boson, neglecting jet masses, and exploiting momentum conservation in the plane transverse to

[2] The parameter $\tilde{d}$ is related to the parameter $\hat{\kappa}_W = \tilde{\kappa}_W / \kappa_{\text{SM}} \tan\alpha$ used in the investigation of CP properties in the decay $H \to WW^*$ via $\tilde{d} = -\hat{\kappa}_W = -\tilde{\kappa}_W / \kappa_{\text{SM}} \tan\alpha$. The choice $\tilde{d} = \tilde{d}_B$ yields $\hat{\kappa}_W = \hat{\kappa}_Z$ as assumed in the combination of the $H \to WW^*$ and $H \to ZZ$ decay analyses [25].

the beam line. The concept of the Optimal Observable combines the information of the seven-dimensional phase space in a single observable, which is shown to have the highest sensitivity for small values of the parameter of interest and neglects contributions proportional to $\tilde{d}^2$ in the matrix element.

The Optimal Observable for the determination of $\tilde{d}$ is given by the ratio of the interference term in the matrix element to the SM contribution:

$$OO = \frac{2\,\mathrm{Re}(\mathcal{M}^*_{\mathrm{SM}}\mathcal{M}_{\mathrm{CP-odd}})}{|\mathcal{M}_{\mathrm{SM}}|^2}\,.$$

In order to make an almost model-independent test of CP invariance, the mean value of the Optimal Observable can be measured. If no CPV is present in the HVV vertex, then the expectation value of the Optimal Observable vanishes: $\langle OO \rangle = 0$, as the Optimal Observable is a CP-odd (and $\hat{\mathrm{T}}$-odd[3]) variable. But since the initial state of VBF production of the Higgs boson is not CP-symmetric, this argument assumes that effects from rescattering are negligible [38]. Thus an observation of a non-vanishing mean value or an asymmetry in the Optimal Observable distribution would indicate physics beyond the SM, either stemming from CPV, or originating from rescattering effects (i.e. new particles being on mass-shell in loop corrections to the HVV vertex). Example distributions of the Optimal Observable for signal events after the full event selection as described in Section 5 are shown for various values of $\tilde{d}$ in Figure 1. In the SM the distribution is symmetric and has a mean value of zero, whereas a non-vanishing value of $\tilde{d}$ causes an asymmetry and a non-vanishing mean value.

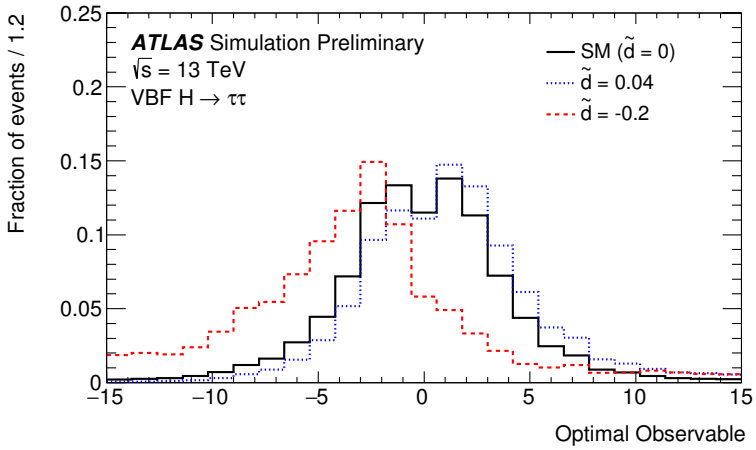

Figure 1: Distribution of the Optimal Observable for signal events for three example values of $\tilde{d}$ after event reconstruction and application of the full event selection used to define the signal region (see Section 5). Non-vanishing values of $\tilde{d}$ cause an asymmetry and a non-vanishing mean value.

The values of the leading-order matrix elements (ME) needed for the calculation of the Optimal Observable are extracted from HAWK [43–45]. The evaluation requires the four-momenta of the Higgs boson and the two tagging jets. The momentum fraction x_1 (x_2) of the initial-state parton from the proton moving in the positive (negative) z-direction (along the beam) can be derived by exploiting energy–momentum conservation from the Higgs boson and tagging jet four-momenta as

$$x^{\mathrm{reco}}_{1,2} = \frac{m_{Hjj}}{\sqrt{s}} \mathrm{e}^{\pm y_{Hjj}},$$

[3] $\hat{\mathrm{T}}$ denotes the naive time reversal according to Ref. [38], which inverts the direction of momenta and spins.

where m_{Hjj} (y_{Hjj}) is the invariant mass (rapidity) obtained from the vectorially summed four-momenta of the tagging jets and the Higgs boson. Since the flavour of the initial- and final-state partons cannot be determined experimentally, the sum over all possible flavour configurations $ij \to klH$ weighted by the CT10 leading-order parton distribution functions (PDFs) [46] is calculated separately for the matrix elements in the numerator and denominator:

$$\begin{aligned} 2\,\mathrm{Re}(\mathcal{M}^{*}_{\mathrm{SM}}\mathcal{M}_{\mathrm{CP-odd}}) &= \sum_{i,j,k,l} f_i(x_1) f_j(x_2) 2\,\mathrm{Re}((\mathcal{M}^{ij\to klH}_{\mathrm{SM}})^{*}\mathcal{M}^{ij\to klH}_{\mathrm{CP-odd}}) \\ |\mathcal{M}_{\mathrm{SM}}|^2 &= \sum_{i,j,k,l} f_i(x_1) f_j(x_2) |\mathcal{M}^{ij\to klH}_{\mathrm{SM}}|^2 \,. \end{aligned}$$

The best estimate and confidence intervals for $\tilde{d}$ in this analysis are determined by a fit of the expected to the measured distribution of the Optimal Observable. It has been shown in Ref. [34] that the Optimal Observable yields a significantly higher sensitivity in the determination of $\tilde{d}$ than the CP-odd "signed" difference in the azimuthal angle between the two tagging jets $\Delta\phi_{jj}$, as suggested in Ref. [42].

3 ATLAS detector

The ATLAS experiment [47–49] at the LHC is a multi-purpose particle detector with a forward–backward symmetric cylindrical geometry and a near 4π coverage in solid angle.[4] It consists of an inner tracking detector surrounded by a thin superconducting solenoid providing a 2 T axial magnetic field, electromagnetic and hadron calorimeters, and a muon spectrometer. The inner tracking detector covers the pseudorapidity range $|\eta| < 2.5$. It consists of silicon pixel, silicon microstrip, and transition radiation tracking detectors. Lead/liquid-argon (LAr) sampling calorimeters provide electromagnetic (EM) energy measurements with high granularity. A hadron (steel/scintillator-tile) calorimeter covers the central pseudorapidity range ($|\eta| < 1.7$). The end-cap and forward regions are instrumented with LAr calorimeters for both EM and hadronic energy measurements up to $|\eta| = 4.9$. The muon spectrometer surrounds the calorimeters and is based on three large air-core toroidal superconducting magnets with eight coils each. The field integral of the toroids ranges between 2.0 and 6.0 T m across most of the detector. The muon spectrometer includes a system of precision tracking chambers and fast detectors for triggering. A two-level trigger system is used to select events. The first-level trigger is implemented in hardware and uses a subset of the detector information to reduce the accepted rate to at most 100 kHz. This is followed by a software-based trigger that reduces the accepted event rate to 1 kHz on average depending on the data-taking conditions.

4 Simulated event samples

Samples of signal and background events are simulated using various Monte Carlo (MC) event generators. The generators and the PDF sets used for the hard-scattering process and the models used for the parton

[4] ATLAS uses a right-handed coordinate system with its origin at the nominal interaction point (IP) in the centre of the detector and the z-axis along the beam pipe. The x-axis points from the IP to the centre of the LHC ring, and the y-axis points upwards. Cylindrical coordinates (r, ϕ) are used in the transverse plane, ϕ being the azimuthal angle around the z-axis. The pseudorapidity is defined in terms of the polar angle θ as $\eta \equiv -\ln\tan(\theta/2)$. Angular distance is measured in units of $\Delta R \equiv \sqrt{(\Delta\eta)^2 + (\Delta\phi)^2}$.

shower, hadronization, and underlying-event activity (UEPS) are summarized in Table 1. In addition, the order of the total cross section calculation is given.

Only Higgs-boson production via VBF is considered as signal, including the $H \to \tau\tau$ decay as well as the $H \to WW^* \to \ell\nu\ell\nu$ decay. The analysis is not sensitive to CPV in the $H \to WW^*$ decay vertex. The other Higgs-boson production modes — gluon–gluon fusion (ggF H), VH, $t\bar{t}H$ — are considered as background in this analysis and all couplings other than the HVV coupling are set to SM values. All SM signal and background samples used in this analysis are the same as those employed in Ref. [39] and the same normalization of those samples is used. The only exception is the normalization of the electroweak Zjj process. Here, the LO cross section calculated by the Sherpa 2.2.1 generator [50–53] is corrected by a factor of 1.7 to match the cross section value measured by the ATLAS experiment at $\sqrt{s} = 13$ TeV [54].

Table 1: Overview of simulation tools used to generate signal and background processes, and to model the UEPS. The PDF sets are also summarized. All Higgs boson events are generated assuming $m_H = 125$ GeV. Alternative event generators and configurations used to estimate systematic uncertainties are shown in parentheses. The prediction order in the last column refers to the cross section used to normalize the event sample.

Process	Matrix element (alternative)	PDF set	UEPS model (alternative model)	Prediction order for total cross-section
VBF H	Powheg-Box v2 [55–59]	PDF4LHC15 NLO [60]	Pythia 8 [61] (Herwig 7 [63, 64])	approx. NNLO QCD + NLO EW [43, 44, 62]
ggF H	Powheg-Box v2 NNLOPS [69–71]	PDF4LHC15 NNLO	Pythia 8 (Herwig 7)	N^{3}LO QCD + NLO EW [65–68]
VH	Powheg-Box v2 [72]	PDF4LHC15 NLO	Pythia 8	$qq/qg \to VH$: NNLO QCD + NLO EW [73, 74] $gg \to ZH$: NLO + NLL QCD [75, 76]
$t\bar{t}H$	MG5_aMC@NLO 2.2.2 [77, 78]	NNPDF3.0LO [79]	Pythia 8	NLO QCD + NLO EW [80–85]
W/Z+jets	Sherpa 2.2.1 [86] (MG5_aMC@NLO 2.2.2)	NNPDF3.0NNLO	Sherpa 2.2.1 [87] (Pythia 8)	NNLO [88, 89]
Electroweak W/Zjj	Sherpa 2.2.1	NNPDF3.0NNLO	Sherpa 2.2.1	LO
$VV/V\gamma^*$	Sherpa 2.2.1	NNPDF3.0NNLO	Sherpa 2.2.1	NLO
$t\bar{t}$	Powheg-Box v2 [90]	CT10 [46]	Pythia 6.428 [91]	NNLO+NNLL [92]
Wt	Powheg-Box v1 [93]	CT10	Pythia 6.428	NLO [93]

To simulate the presence of non-vanishing values of $\tilde{d}$ in the HVV vertex, a matrix element reweighting method is applied to the VBF SM signal sample. The weight is defined as the ratio of the squared ME value of the VBF process associated with a specific amount of CP mixing (given in terms of $\tilde{d}$) to the one obtained from the SM. To extract the weights, the leading order MEs from HAWK are used for the $2 \to 2 + H$ or $2 \to 3 + H$ processes separately. The MEs are evaluated using the four-momenta and particle identification codes of the initial- and final-state partons and the Higgs boson of each event. The reweighting procedure has been validated in Ref. [34] against samples generated with MadGraph5_aMC@NLO [94] and proves to be a good approximation of a full NLO description of the process with non-vanishing values of $\tilde{d}$.

For all samples, a full simulation of the ATLAS detector response [95] using the Geant 4 program [96] is performed. The effect of multiple pp interactions in the same and neighbouring bunch crossings (pileup) is included by overlaying minimum-bias events simulated with Pythia 8 using the MSTW2008LO PDF [97] and the A2 set [98] of tuned parameters on each generated signal and background event. The number of overlaid events is chosen such that the distribution of the average number of interactions per pp bunch crossing in the simulation matches that observed in data.

Table 2: Summary of the event selection requirements for the four analysis channels. In the case of the p_{T} requirements on the τ-lepton decay candidates, the asterisk marks the lowest p_{T} threshold, which increases depending on the trigger used. Details of this are given in Ref. [39]. The transverse momentum of the τ-lepton candidate with the higher (lower) p_{T} is denoted as $p_{\mathrm{T}}^{\tau_1}$ ($p_{\mathrm{T}}^{\tau_2}$). The input variables used for the BDT training and the $\mathrm{BDT}_{\mathrm{score}}$ threshold used to define the signal regions are also reported.

Channel	$\tau_{\mathrm{lep}}\tau_{\mathrm{lep}}$ SF	$\tau_{\mathrm{lep}}\tau_{\mathrm{lep}}$ DF	$\tau_{\mathrm{lep}}\tau_{\mathrm{had}}$	$\tau_{\mathrm{had}}\tau_{\mathrm{had}}$
Preselection	Two isolated τ-lepton decay candidates with opposite electric charge			
	$p_{\mathrm{T}}^{\tau_1} > 19^*/15^*$ GeV (μ/e)	$p_{\mathrm{T}}^{e} > 18$ GeV	$p_{\mathrm{T}}^{\tau_{\mathrm{had}}} > 30$ GeV	$p_{\mathrm{T}}^{\tau_1} > 40$ GeV
	$p_{\mathrm{T}}^{\tau_2} > 10/15^*$ GeV (μ/e)	$p_{\mathrm{T}}^{\mu} > 14$ GeV	$p_{\mathrm{T}}^{\tau_{\mathrm{lep}}} > 21^*$ GeV	$p_{\mathrm{T}}^{\tau_2} > 30$ GeV
	$m_{\tau\tau}^{\mathrm{coll}} > m_Z - 25$ GeV		$m_{\mathrm{T}} < 70$ GeV	$0.8 < \Delta R_{\tau\tau} < 2.5$
	$30 < m_{\ell\ell} < 75$ GeV	$30 < m_{\ell\ell} < 100$ GeV		$\lvert\Delta\eta_{\tau\tau}\rvert < 1.5$
	$E_{\mathrm{T}}^{\mathrm{miss}} > 55$ GeV	$E_{\mathrm{T}}^{\mathrm{miss}} > 20$ GeV		$E_{\mathrm{T}}^{\mathrm{miss}} > 20$ GeV
	$E_{\mathrm{T}}^{\mathrm{miss,\,hard}} > 55$ GeV			
	$N_{b\text{-jets}} = 0$			
VBF topology	$N_{\mathrm{jets}} \geq 2$, $p_{\mathrm{T}}^{j_2} > 30$ GeV, $m_{jj} > 300$ GeV, $\lvert\Delta\eta_{jj}\rvert > 3$			
	$p_{\mathrm{T}}^{j_1} > 40$ GeV			$p_{\mathrm{T}}^{j_1} > 70$ GeV, $\lvert\eta_{j_1}\rvert < 3.2$
BDT input variables	$m_{\tau\tau}^{\mathrm{MMC}}$, m_{jj}, $\Delta R_{\tau\tau}$, $C_{jj}(\tau_1)$, $C_{jj}(\tau_2)$, $p_{\mathrm{T}}^{\mathrm{tot}}$			
	$m_{\tau\tau}^{\mathrm{vis}}$, $m_{\mathrm{T}}^{\tau_1,E_{\mathrm{T}}^{\mathrm{miss}}}$, $p_{\mathrm{T}}^{j_3}$		$C(\phi^{\mathrm{miss}})/\sqrt{2}$	
	$\Delta\phi_{\tau\tau}$	$E_{\mathrm{T}}^{\mathrm{miss}}/p_{\mathrm{T}}^{\tau_1}$, $E_{\mathrm{T}}^{\mathrm{miss}}/p_{\mathrm{T}}^{\tau_2}$	$m_{\tau\tau}^{\mathrm{vis}}$, $\lvert\Delta\eta_{\tau\tau}\rvert$	$p_{\mathrm{T}}^{\tau\tau E_{\mathrm{T}}^{\mathrm{miss}}}$, $\lvert\Delta\eta_{\tau\tau}\rvert$
Signal region	$\mathrm{BDT}_{\mathrm{score}} > 0.78$		$\mathrm{BDT}_{\mathrm{score}} > 0.86$	$\mathrm{BDT}_{\mathrm{score}} > 0.87$

5 Event selection

In this analysis, events with at least two jets and a $H \to \tau\tau$ decay candidate in the final state are selected. All combinations of leptonic ($\tau \to \ell\nu\bar{\nu}$ with $\ell = e, \mu$) and hadronic ($\tau \to$ hadrons ν) τ decays are considered. In the following, the event preselection, which closely follows Ref. [39], is summarized and the analysis strategy using gradient boosted decision trees (BDTs) [99] is described. After data quality requirements, the integrated luminosity of the $\sqrt{s} = 13$ TeV dataset used is 36.1 fb^{-1}. The definition of the physics objects as well as the triggers used in this analysis correspond to those used in Ref. [39], where more details are given.

Depending on the reconstructed decay modes of the two τ leptons, events are separated into four analysis channels: the dileptonic same-flavour ($\tau_{\mathrm{lep}}\tau_{\mathrm{lep}}$ SF), the dileptonic different flavour ($\tau_{\mathrm{lep}}\tau_{\mathrm{lep}}$ DF), the semileptonic ($\tau_{\mathrm{lep}}\tau_{\mathrm{had}}$), and the fully hadronic ($\tau_{\mathrm{had}}\tau_{\mathrm{had}}$) channel. All channels require an exact number of identified and isolated τ-lepton decay candidates, i.e. electrons, muons, and visible decay products of hadronic τ decays ($\tau_{\text{had-vis}}$), as defined in Ref. [39], corresponding to their respective final state. Events with additional τ-lepton decay candidates are rejected. This ensures that the selected data samples in the four channels do not overlap. The two τ-lepton decay candidates are required to be of opposite electric charge and to fulfill the requirements on the transverse momentum given in Table 2.

The event selection for the four analysis channels is summarized in Table 2. In the $\tau_{\mathrm{lep}}\tau_{\mathrm{lep}}$ and $\tau_{\mathrm{had}}\tau_{\mathrm{had}}$ channels, only events with missing transverse momentum $E_{\mathrm{T}}^{\mathrm{miss}} > 20$ GeV are selected to reject events without neutrino candidates. To suppress the large background from $Z \to \ell\ell$ production in the $\tau_{\mathrm{lep}}\tau_{\mathrm{lep}}$ SF channel, requirements are tightened on the $E_{\mathrm{T}}^{\mathrm{miss}}$. Furthermore, an additional requirement is introduced on the $E_{\mathrm{T}}^{\mathrm{miss,\,hard}}$ quantity, an $E_{\mathrm{T}}^{\mathrm{miss}}$ calculation considering only contributions from physics objects and neglecting contributions from inner detector tracks originating from the vertex of the hard-scattering

process, but not associated with any of the reconstructed objects. In addition, a requirement on the invariant mass of the two light leptons, $m_{\ell\ell}$, is applied in the $\tau_{\text{lep}}\tau_{\text{lep}}$ channels. A requirement on the di-τ mass calculated in the collinear approximation [100] of $m_{\tau\tau}^{\text{coll}} > m_Z - 25\,\text{GeV}$ is introduced in the $\tau_{\text{lep}}\tau_{\text{lep}}$ channels to ensure orthogonality between this analysis and the analysis of $H \to WW^* \to \ell\nu\ell\nu$ [101], which has a similar final state. In the $\tau_{\text{lep}}\tau_{\text{lep}}$ and $\tau_{\text{lep}}\tau_{\text{had}}$ channels, the top-quark background is suppressed by requiring that no jet with $p_{\text{T}} > 25\,\text{GeV}$ and $|\eta| < 2.5$ contains b-hadrons (b-jets). A multivariate algorithm [102, 103] is used to identify and select b-jets with a working point corresponding to an average efficiency of 85%, as measured on a sample from top-quark pair production. Low transverse mass[5] ($m_{\text{T}} < 70\,\text{GeV}$) is required in the $\tau_{\text{lep}}\tau_{\text{had}}$ channel to reject events with leptonic W decays. Requirements on the angular distance between the visible decay products of the two selected τ-lepton decays, $\Delta R_{\tau\tau}$, and their pseudorapidity difference, $|\Delta\eta_{\tau\tau}|$, are applied in the $\tau_{\text{had}}\tau_{\text{had}}$ channel to reject non-resonant background events.

To select Higgs boson events produced by VBF, all channels require at least two jets with transverse momentum of the leading jet $p_{\text{T}}^{j_1} > 40\,\text{GeV}$ and of the subleading jet $p_{\text{T}}^{j_2} > 30\,\text{GeV}$, a large invariant mass of the two leading jets, $m_{jj} > 300\,\text{GeV}$, and a pseudorapidity separation of $|\Delta\eta_{jj}| > 3$. In the $\tau_{\text{had}}\tau_{\text{had}}$ channel, the requirements on the leading jet are raised to $p_{\text{T}}^{j_1} > 70\,\text{GeV}$ and $|\eta_{j_1}| < 3.2$ to achieve a uniform trigger selection efficiency. This selection is denoted as the VBF event selection in the following.

To construct a signal region enriched in VBF signal events, BDTs trained to discriminate between the VBF signal and backgrounds are used in all channels. Kinematic variables used in the BDT training can be categorized as follows:

- properties of the Higgs boson which discriminate against all background processes without a Higgs boson: the visible mass of the di-τ system, $m_{\tau\tau}^{\text{vis}}$, the transverse momentum of the $\tau\tau E_{\text{T}}^{\text{miss}}$ system, $p_{\text{T}}^{\tau\tau E_{\text{T}}^{\text{miss}}}$, and the reconstructed Higgs boson mass, $m_{\tau\tau}^{\text{MMC}}$, determined using the missing-mass calculator (MMC) [104].
- properties of a resonant di-τ decay which discriminate against processes with mis-identified τ-decay candidates: the angular distance $\Delta R_{\tau\tau}$, the difference in pseudorapidity $|\Delta\eta_{\tau\tau}|$, and the difference in azimuth $\Delta\phi_{\tau\tau}$ between the two visible τ leptons. Furthermore, the azimuthal centrality of $E_{\text{T}}^{\text{miss}}$, $C(\phi^{\text{miss}})/\sqrt{2}$, that quantifies the relative angular position of the missing transverse momentum with respect to the visible τ-decay products in the transverse plane, is constructed[6]. In addition, the transverse momentum ratio $E_{\text{T}}^{\text{miss}}/p_{\text{T}}^{\tau_1}$ ($E_{\text{T}}^{\text{miss}}/p_{\text{T}}^{\tau_2}$) between the $E_{\text{T}}^{\text{miss}}$ and the leading (subleading) τ-candidate as well as the transverse mass of the $E_{\text{T}}^{\text{miss}}$ and the leading τ-candidate, $m_{\text{T}}^{\tau_1, E_{\text{T}}^{\text{miss}}}$, are used.
- properties of the VBF topology: m_{jj}, the total transverse momentum $p_{\text{T}}^{\text{tot}}$, which is defined as the transverse momentum of the system composed of all objects in a VBF event (τ_1, τ_2, j_1, j_2, $E_{\text{T}}^{\text{miss}}$), η-centralities, $C_{jj}(\tau_1)$ and $C_{jj}(\tau_2)$, of each τ-candidate relative to the pseudorapidity of the two leading jets[7], and the transverse momentum of the third leading jet $p_{\text{T}}^{j_3}$ which is set to zero for events

[5] The transverse mass is defined as $m_{\text{T}} = \sqrt{2 p_{\text{T}}^{\ell} E_{\text{T}}^{\text{miss}} \cdot (1 - \cos\Delta\phi)}$, where $\Delta\phi$ is the azimuthal separation between the directions of the lepton and the missing transverse momentum.

[6] $C(\phi^{\text{miss}})$ is defined as $(A+B)/\sqrt{A^2+B^2}$, where $A = \sin(\phi_{E_{\text{T}}^{\text{miss}}} - \phi_{\tau_2})/\sin(\phi_{\tau_1} - \phi_{\tau_2})$ and $B = \sin(\phi_{\tau_1} - \phi_{E_{\text{T}}^{\text{miss}}})/\sin(\phi_{\tau_1} - \phi_{\tau_2})$.

[7] $C_{jj}(\tau) = \exp\left[\frac{-4}{(\eta_{j_1} - \eta_{j_2})^2}\left(\eta_\tau - \frac{\eta_{j_1}+\eta_{j_2}}{2}\right)^2\right]$, where η_τ, η_{j_1} and η_{j_2} are the pseudorapidities of the τ-candidate and the two leading jets, respectively. This variable has a value of unity when the object is halfway in η between the two jets, 1/e when the

with exactly two jets.

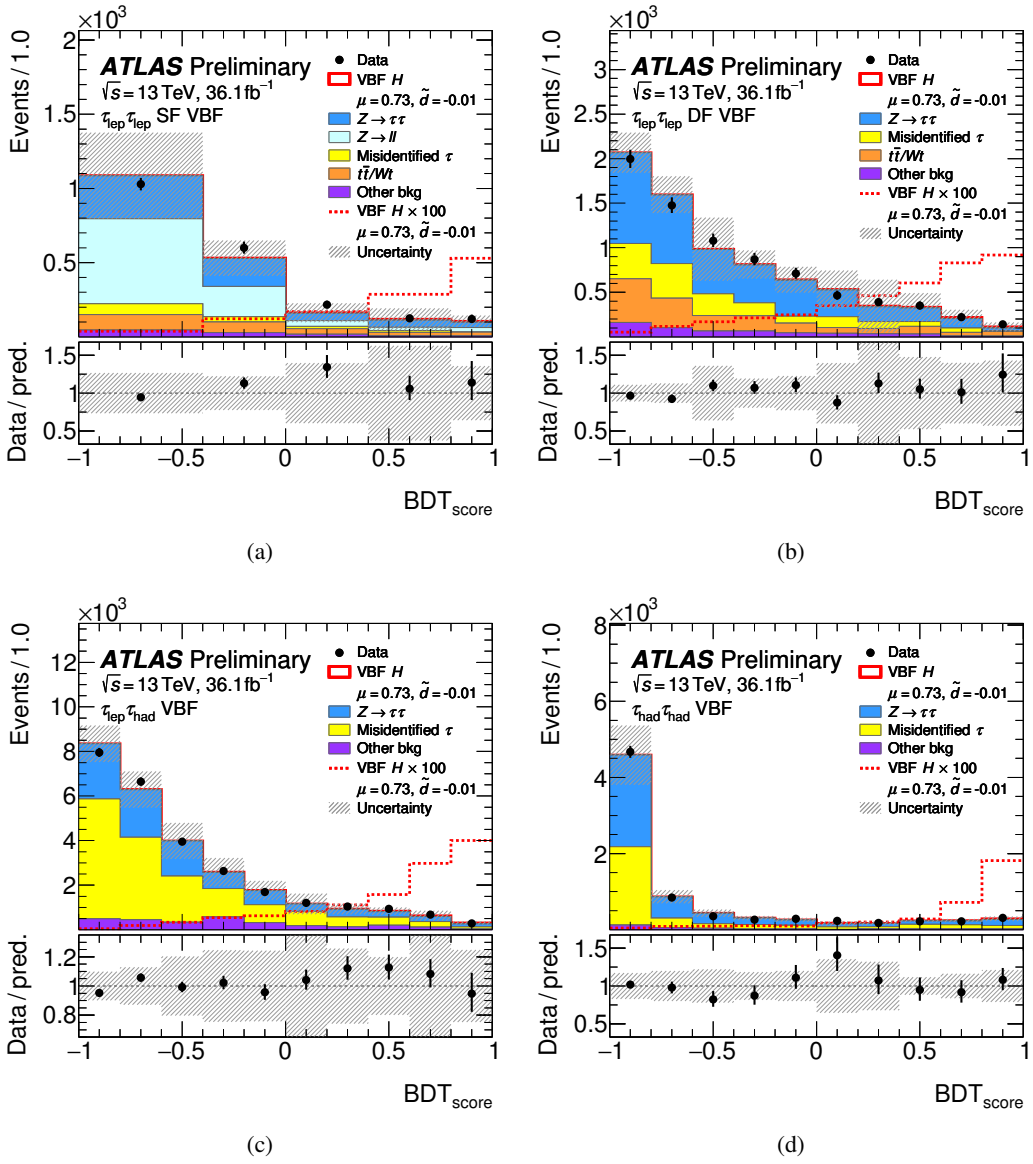

Figure 2: Post-fit $\text{BDT}_{\text{score}}$ distributions after the VBF event selection for the (a) $\tau_{\text{lep}}\tau_{\text{lep}}$ SF, (b) $\tau_{\text{lep}}\tau_{\text{lep}}$ DF , (c) $\tau_{\text{lep}}\tau_{\text{had}}$ and (d) $\tau_{\text{had}}\tau_{\text{had}}$ analysis channels. The ratios of the data to the prediction are shown in the lower panels. The observed VBF signal ($\mu = 0.73$, $\tilde{d} = -0.01$) is shown with the solid red line on the top of the histogram stack. "Other bkg" denotes all background contributions not listed explicitly in the legend. The dashed line shows the observed VBF signal scaled up by a factor of 100, and is not part of the histogram stack. The size of the combined statistical, experimental, and theoretical uncertainties in the background is indicated by the hatched bands.

The most important variables in the training are $m_{\tau\tau}^{\text{MMC}}$, m_{jj}, and $C_{jj}(\tau_1)$. The resulting BDT score ($\text{BDT}_{\text{score}}$) distributions are shown in Figure 2 for events surviving the VBF event selection and show the ability of the BDT to separate the signal process from background processes (discussed in Section 6). All figures in this letter use signal strength μ (defined as the ratio of the measured cross section times branching

object is aligned with one of the jets, and $< 1/\text{e}$ when the object is not between the jets in η.

ratio to the SM prediction for the VBF signal process), background normalizations, and systematic uncertainties as fitted by the final statistical analysis discussed in Section 8 and referred to as *post-fit*. The signal purity increases at high values of $\mathrm{BDT}_{\mathrm{score}}$. A threshold on $\mathrm{BDT}_{\mathrm{score}}$ is used to define the final signal region (SR) in each channel. This threshold is chosen to yield a high signal significance and is given in Table 2 for each channel. The signal efficiency of the selection with respect to the VBF event selection is 32% (27%) for the $\tau_{\mathrm{lep}}\tau_{\mathrm{lep}}$ SF ($\tau_{\mathrm{lep}}\tau_{\mathrm{lep}}$ DF) channel, 29% for the $\tau_{\mathrm{lep}}\tau_{\mathrm{had}}$ channel, and 49% for the $\tau_{\mathrm{had}}\tau_{\mathrm{had}}$ channel. The efficiency for the sum of background processes, on the other hand, is 1.5% (0.8%) for the $\tau_{\mathrm{lep}}\tau_{\mathrm{lep}}$ SF ($\tau_{\mathrm{lep}}\tau_{\mathrm{lep}}$ DF) channel, 0.4% for the $\tau_{\mathrm{lep}}\tau_{\mathrm{had}}$ channel, and 1.1% for the $\tau_{\mathrm{had}}\tau_{\mathrm{had}}$ channel. In each SR the Optimal Observable is then used to probe for CPV. No dependence of the mean values of the Optimal Observable on $\mathrm{BDT}_{\mathrm{score}}$ is observed, confirming that the SR selection criteria do not introduce a CP asymmetry.

6 Background estimation

Several background processes contribute to the SR event yields in the four analysis channels. The dominant contributions in the $\tau_{\mathrm{lep}}\tau_{\mathrm{lep}}$ DF, $\tau_{\mathrm{lep}}\tau_{\mathrm{had}}$, and $\tau_{\mathrm{had}}\tau_{\mathrm{had}}$ channels arise from $Z \to \tau\tau$ production and from light- and heavy-flavour jets that are misidentified as prompt leptonic or hadronic τ decays (denoted as "Misidentified τ"). The misidentified τ decays in the $\tau_{\mathrm{lep}}\tau_{\mathrm{lep}}$ and $\tau_{\mathrm{lep}}\tau_{\mathrm{had}}$ channels originate largely from W+jets production with smaller contributions from multijet and top-quark production, while in the $\tau_{\mathrm{had}}\tau_{\mathrm{had}}$ channel the contribution from multijet production dominates. In the $\tau_{\mathrm{lep}}\tau_{\mathrm{lep}}$ SF channel the contribution from $Z \to \ell\ell$ production is dominant. Other background contributions in all analysis channels originate from top-quark pair and associated Wt production (denoted as "$t\bar{t}/Wt$" in the following), diboson production, and other Higgs boson production modes.

Background contributions with prompt leptonic or hadronic τ decays are estimated from simulation, while the estimation of the background contribution from misidentified τ decays is mostly data-driven [39]. Dedicated control regions (CR) are defined in data to normalize the predictions of the following background processes: $Z \to \tau\tau$ (for all channels), $t\bar{t}/Wt$ and $Z \to \ell\ell$ (only for the $\tau_{\mathrm{lep}}\tau_{\mathrm{lep}}$ channels), and the misidentified τ decays (only for the $\tau_{\mathrm{had}}\tau_{\mathrm{had}}$ channel). All other background processes with prompt τ decays (including other Higgs boson production modes) are normalized to their SM prediction.

To construct a CR for $Z \to \tau\tau$ production, the SR requirement on the $\mathrm{BDT}_{\mathrm{score}}$ (given in Table 2) is inverted for each analysis channel. This CR is denoted low-$\mathrm{BDT}_{\mathrm{score}}$ CR in the following. As the purity of $Z \to \tau\tau$ production in the low-$\mathrm{BDT}_{\mathrm{score}}$ CR ranges from 30–54% depending on the analysis channel, $Z \to \tau\tau$ production is normalized to data in the Z boson mass peak of the $m_{\tau\tau}^{\mathrm{MMC}}$ distributions, shown in Figure 3. In the fit, discussed in Section 8, the $Z \to \tau\tau$ normalization is correlated across all analysis channels and the fit yields a normalization factor of 0.93 ± 0.08. To ensure that the normalization is valid in the SR, the modelling of the Z-boson and jet kinematic properties has been checked in a validation region which is composed of $Z \to \ell\ell$ events with kinematic properties similar to those of the $Z \to \tau\tau$ events in the VBF region of each analysis channel. This region is defined by selecting two same-flavour leptons of opposite charge with a dilepton mass of $m_{\ell\ell} > 80\,\mathrm{GeV}$ and low missing transverse momentum ($E_{\mathrm{T}}^{\mathrm{miss}} < 55\,\mathrm{GeV}$). All VBF selection requirements given in Table 2 are applied as well. As in Ref. [39], a slight positive slope in the ratio of data to the Sherpa simulation as a function of m_{jj} is observed. In this analysis, the simulated $Z \to \tau\tau$ and $Z \to \ell\ell$ events are reweighted to the observed m_{jj} distribution after the VBF event selection, which results in a small change in the acceptance of $Z \to \tau\tau$ and $Z \to \ell\ell$ events in the SR.

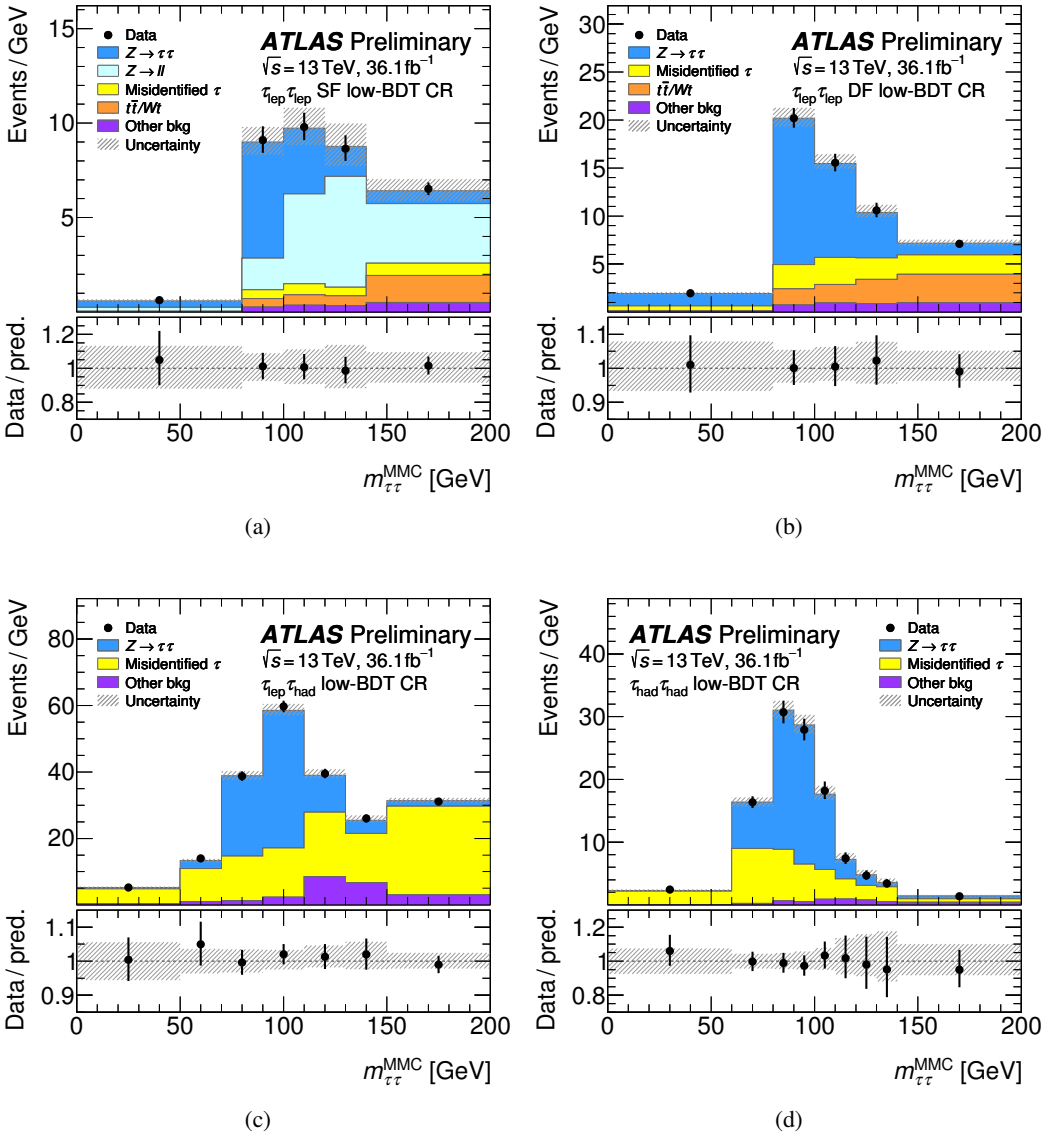

Figure 3: Post-fit $m_{\tau\tau}^{\text{MMC}}$ distributions in the low-BDT$_{\text{score}}$ CR for the (a) $\tau_{\text{lep}}\tau_{\text{lep}}$ SF, (b) $\tau_{\text{lep}}\tau_{\text{lep}}$ DF , (c) $\tau_{\text{lep}}\tau_{\text{had}}$ and (d) $\tau_{\text{had}}\tau_{\text{had}}$ analysis channels. The ratios of the data to the prediction are shown in the lower panels. The signal contamination in the CR is negligible. "Other bkg" denotes all background contributions not listed explicitly in the legend. The size of the combined statistical, experimental, and theoretical uncertainties in the background is indicated by the hatched bands.

In each of the two $\tau_{\text{lep}}\tau_{\text{lep}}$ channels, a top-quark CR is defined by inverting the veto on b-tagged jets and not applying the selection on the BDT$_{\text{score}}$. The normalization of $t\bar{t}/Wt$ production is constrained by the event yield in these CRs, corresponding to a normalization of 1.16 ± 0.06 from the combined fit to data. Additionally, another CR is defined to normalize the $Z \to \ell\ell$ process for the $\tau_{\text{lep}}\tau_{\text{lep}}$ SF channel. Again, the selection on the BDT$_{\text{score}}$ is not applied, and the requirement on the dilepton invariant mass is changed to $80 < m_{\ell\ell} < 100\,\text{GeV}$. The observed event yield in the $Z \to \ell\ell$ CR constrains the normalization of simulated $Z \to \ell\ell$ events in the $\tau_{\text{lep}}\tau_{\text{lep}}$ SF channel to 1.0 ± 0.4.

In the $\tau_{\text{had}}\tau_{\text{had}}$ channel, the background from mis-identified hadronic τ decays is dominated by multijet events. This background process is modelled using a template extracted from $\tau_{\text{had-vis}}$ candidates with one, two, or three associated tracks that pass all selection requirements, but fail the opposite-charge requirement. Before the final fit, the template is normalized to data by a fit of the $|\Delta\eta_{\tau\tau}|$ distribution after the preselection, but removing the requirement on $|\Delta\eta_{\tau\tau}|$. In the final fit the template is normalized to data in the $m_{\tau\tau}^{\text{MMC}}$ distribution of the low-BDT$_{\text{score}}$ CR in the $\tau_{\text{had}}\tau_{\text{had}}$ channel. Then, the multijet background is normalized with a factor of 0.99 ± 0.09 with respect to the pre-fit normalization.

The modelling of the Optimal Observable distribution for the background processes is validated in all CRs. Figure 4 shows Optimal Observable distributions in the low-BDT$_{\text{score}}$ CR for all analysis channels where the background processes have been normalized to the result of the fit. The data and the predicted distributions are observed to be compatible within uncertainties here as well as in the top-quark and $Z \to \ell\ell$ CRs of the $\tau_{\text{lep}}\tau_{\text{lep}}$ channels. Distributions for the top-quark and $Z \to \ell\ell$ CRs are shown in the Appendix.

7 Systematic uncertainties

The effects of the systematic uncertainties on the yields in both the SRs and CRs and on the shape of the Optimal Observable in the SRs, as well as the $m_{\tau\tau}^{\text{MMC}}$ distributions in the CRs, are evaluated following the procedures in Ref. [39]. The sources of uncertainty can be grouped into two categories: experimental and theoretical. The dominant experimental uncertainties stem from the determination of jet energy resolution and scale [105, 106] and of the $\tau_{\text{had-vis}}$ energy scale and resolution [107], as well as of the $\tau_{\text{had-vis}}$ reconstruction and identification efficiencies [108]. Other sources of uncertainty are lepton energy (momentum) scale and resolution, identification and isolation [109–111], missing transverse momentum reconstruction [112], b-tagging efficiency [102, 103], modelling of pile-up, and luminosity measurement [113]. The luminosity uncertainty is only applied to the VBF signal and to background processes normalized to theoretical predictions. Uncertainties on backgrounds from misidentified τ-leptons arise from limited statistics of the data-driven templates and corrections used, from closure tests performed in regions where the τ-leptons are required to have the same charge, and from the subtraction of the electroweak contributions.

Theoretical uncertainties on the total cross section are evaluated for the Higgs boson production cross sections for ggF H, VH, and $t\bar{t}H$ production by varying the QCD factorization and renormalization scales as well as the PDF model following the recommendations in Ref. [114]. Also, uncertainties in the $H \to \tau\tau$ and $H \to WW^*$ branching ratios are considered [114]. Theoretical uncertainties on the MC modelling are considered for the VBF and gluon–gluon fusion production of the Higgs-boson as well as for $Z \to \tau\tau$ production. For all simulated background contributions, other than $Z \to \tau\tau$, no theoretical uncertainties are considered, as their impact is negligible. Uncertainties on MC modelling are assessed by a comparison between nominal and alternative event generators and UEPS models, as indicated in Table 1. In addition, the effects of QCD factorization and renormalization scale variations, matching scale variations (in case of $Z \to \tau\tau$ only), and PDF model uncertainties are evaluated. As an additional uncertainty on the $Z \to \tau\tau$ and $Z \to \ell\ell$ processes, the full difference between the sample reweighted to the observed m_{jj} distribution and the sample without reweighting is applied to the full analysis. An uncertainty to account for the signal reweighting procedure described in Section 4 has been considered and found to be negligible. The uncertainty due to limited MC statistics is evaluated for the sum of all MC-based background processes in each analysis bin.

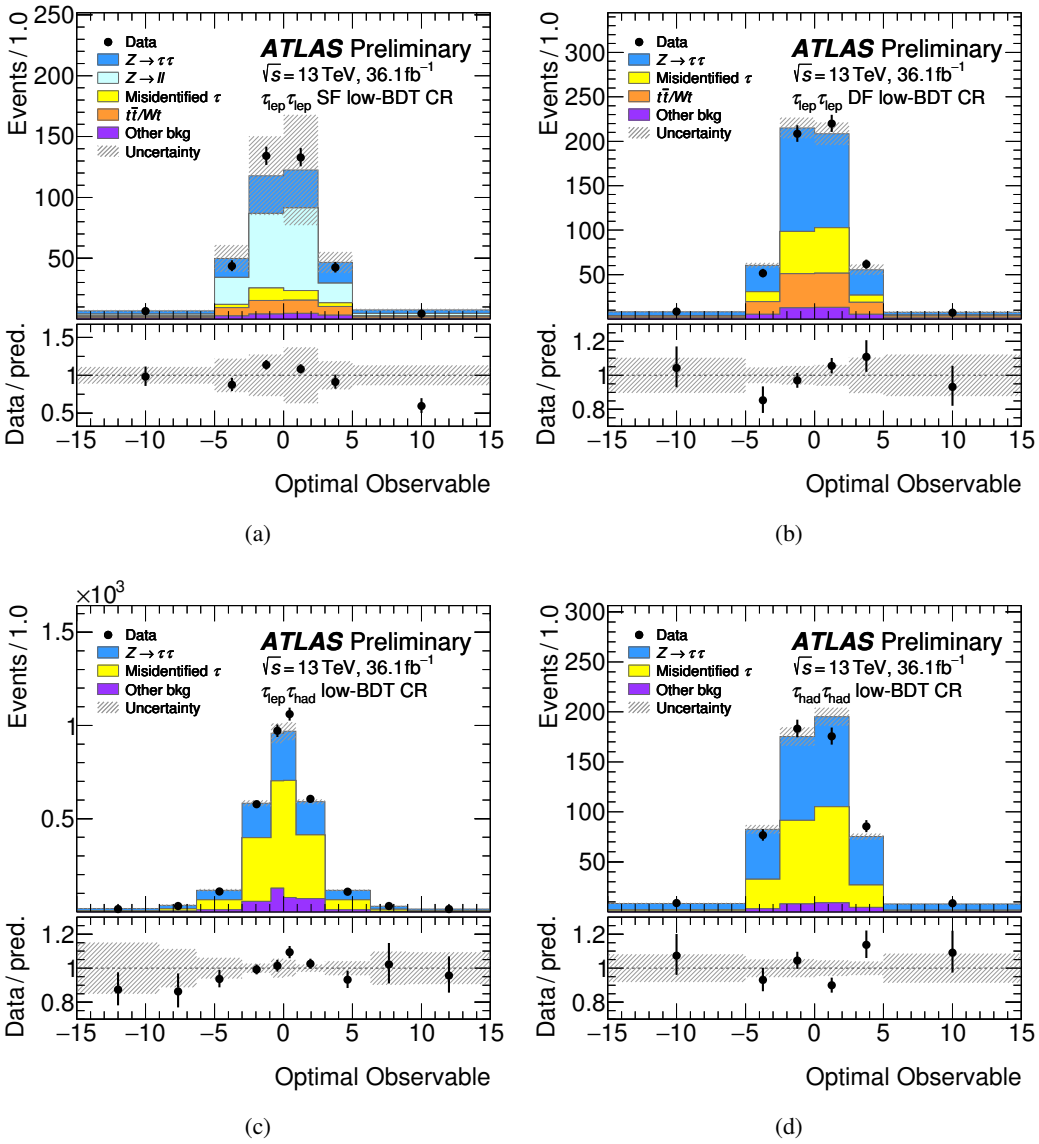

Figure 4: Post-fit Optimal Observable distributions in the low-BDT$_{\text{score}}$ CR for the (a) $\tau_{\text{lep}}\tau_{\text{lep}}$ SF, (b) $\tau_{\text{lep}}\tau_{\text{lep}}$ DF , (c) $\tau_{\text{lep}}\tau_{\text{had}}$ and (d) $\tau_{\text{had}}\tau_{\text{had}}$ analysis channels. The ratios of the data to the prediction are shown in the lower panels. The signal contamination in the CR is negligible. "Other bkg" denotes all background contributions not listed explicitly in the legend. The size of the combined statistical, experimental, and theoretical uncertainties in the background is indicated by the hatched bands.

8 Fitting procedure

The best estimate of $\tilde{d}$ is obtained using a binned maximum-likelihood fit (ML-fit) simultaneously performed on the SRs and all introduced CRs, included in order to constrain background normalizations and nuisance parameters describing the systematic uncertainties. The ML-fit uses the distribution of the Optimal Observable in the four high BDT$_{\text{score}}$ SRs, one for each analysis channel. The $m_{\tau\tau}^{\text{MMC}}$ distributions in the low BDT$_{\text{score}}$ region for each channel are included in the ML-fit, as well as the event yields in the $Z \to \ell\ell$

($\tau_{\text{lep}}\tau_{\text{lep}}$ SF) and top-quark ($\tau_{\text{lep}}\tau_{\text{lep}}$ SF and DF) CRs.

The inclusion of the $m_{\tau\tau}^{\text{MMC}}$ distributions in the low $\text{BDT}_{\text{score}}$ regions provides the main constraint on the $Z \to \tau\tau$ normalization which is free to float in the ML-fit. The $Z \to \ell\ell$ background in the $\tau_{\text{lep}}\tau_{\text{lep}}$ SF channel and top quark backgrounds in the $\tau_{\text{lep}}\tau_{\text{lep}}$ SF and DF channels are also free to float and their contributions are constrained by the inclusion of CRs in the ML-fit.

The normalization of the signal is unconstrained in the ML-fit such that the analysis only exploits the shape of the distribution of the Optimal Observable in the estimate of $\tilde{d}$. Any possible model-dependence of the cross section on CP-mixing scenarios is not exploited. The relative proportion of the two Higgs boson decay modes ($H \to \tau\tau$ and $H \to WW^*$) in the signal (relevant only for the $\tau_{\text{lep}}\tau_{\text{lep}}$ channel) is assumed to be correctly predicted by the SM. All other Higgs boson production modes for these decays are considered as background and are normalized to their SM predicted yields.

The ML-fit uses a binned likelihood function $\mathcal{L}(\boldsymbol{x}; \mu, \boldsymbol{\theta})$, which is a function of the data $\boldsymbol{x}$, the free-floating signal strength μ, and nuisance parameters $\boldsymbol{\theta}$ corresponding to the systematic uncertainties mentioned in Section 7. The likelihood function is evaluated for each $\tilde{d}$ hypothesis using the relevant reweighted signal templates defined in Section 4, with the background model unchanged, and a negative log-likelihood (NLL) curve can then be constructed as a function of $\tilde{d}$.

The best estimator for the parameter of interest $\tilde{d}$ is obtained at the point where the NLL curve reaches a minimum. Central confidence intervals can be placed by reading off the points on the NLL curve which exceed the minimum value by a certain threshold.

9 Results

For a CP-even Higgs boson, the mean value of the Optimal Observable for the signal and background processes is expected to be zero under the assumption that any effects from the rescattering of new particles in loops can be neglected. However, CP-violating effects could result in the mean value of the Optimal Observable in data deviating from zero, allowing for an almost model-independent test for CP-violating effects in this measurement.

The observed values for the mean of the Optimal Observable in data, along with their statistical uncertainties, are summarized in Table 3 for the four channels in this analysis, as well as their combination. These values are fully consistent with zero, and no evidence of CPV is observed.

Table 3: Mean values of the Optimal Observable with statistical uncertainties that are observed in data for the four analysis channel SRs and their combination.

Channel	⟨Optimal Observable⟩
$\tau_{\text{lep}}\tau_{\text{lep}}$ SF	-0.54 ± 0.72
$\tau_{\text{lep}}\tau_{\text{lep}}$ DF	0.71 ± 0.81
$\tau_{\text{lep}}\tau_{\text{had}}$	0.74 ± 0.78
$\tau_{\text{had}}\tau_{\text{had}}$	-1.13 ± 0.65
Combined	-0.19 ± 0.37

To extract confidence intervals on the CP-mixing parameter $\tilde{d}$, the ML-fit described in Section 8 is carried out. The post-fit distributions of the Optimal Observable in the various analysis channels are shown

in Figure 5. Here the value of the parameter of interest, $\tilde{d}$, along with the nuisance parameters and normalizations of the signal and background processes, have been adjusted within their allowed constraints to minimize the NLL curve. Values of the NLL are evaluated in steps of $\Delta\tilde{d} = 0.01$, and the smallest value of the NLL is observed at $\tilde{d} = -0.01$. This is the value of $\tilde{d}$ that is used for the post-fit distributions and event yields. Based upon interpolations between the discrete evaluation of the various NLL values as a function of $\tilde{d}$, the best estimator for $\tilde{d}$ is $-0.013^{+0.048}_{-0.077}$. This value is consistent with the SM expectation of zero, and no evidence of CPV is observed using this approach. The best-fit signal strength from the ML-fit is $\mu = 0.73 \pm 0.47$.

While the predicted background distributions for the Optimal Observable are not perfectly symmetric, they are statistically consistent with a symmetric distribution. This slight asymmetry can cause expected confidence intervals on $\tilde{d}$ to also be asymmetric.

Tables 4 and 5 display the fitted event yields of the signal ($\mu = 0.73$, $\tilde{d} = -0.01$) and various background processes for the SRs of each channel, along with the corresponding number of events observed in data. For reference, the signal yields for the SM expectation ($\mu = 1$, $\tilde{d} = 0$) are also shown.

The observed and expected ΔNLL curves are shown in Figure 6(a) as a function of $\tilde{d}$. The expected curves are obtained in a two-step process: firstly, nuisance parameters and background normalization factors are constrained via a ML-fit to all analysis CRs, excluding the SRs; then another fit is performed in all SRs and CRs to pseudo-data which were created with the best-fit parameter values from the first step. This two-step process ensures that the nuisance parameters and the background normalization factors for the expected sensitivity are set to values that are consistent with the observed data in the analysis CRs. The expected ΔNLL curve is shown for $\tilde{d} = 0$ and $\mu = 1$, and represents the best estimate of the sensitivity of the analysis based on SM expectations. Another ΔNLL curve with $\tilde{d} = 0$ and the signal strength μ set to the observed value of 0.73 is also shown in order to demonstrate the decrease in sensitivity due to the lower than expected event yields (see Tables 4 and 5). Also shown for comparison in Figure 6(a) is the pre-fit expected ΔNLL curve, which is obtained using a pseudo-dataset where the event yields and distributions in the SRs and CRs are set to the SM expectations for both signal (with $\tilde{d} = 0$ and $\mu = 1$) and background processes. This demonstrates that the preferred values of the nuisance parameters and

Table 4: Post-fit event yields in the SRs for the $\tau_{\text{lep}}\tau_{\text{lep}}$ (SF) and $\tau_{\text{lep}}\tau_{\text{lep}}$ (DF) analysis channels. The $Z \to \ell\ell$ and diboson backgrounds are grouped together in a single background category for the $\tau_{\text{lep}}\tau_{\text{lep}}$ (DF) channel. For comparison, the expected signal yields for the SM expectation ($\mu = 1$, $\tilde{d} = 0$) are also shown.

Process	$\tau_{\text{lep}}\tau_{\text{lep}}$ SF	$\tau_{\text{lep}}\tau_{\text{lep}}$ DF
Data	26	30
VBF $H \to \tau\tau/WW$ ($\mu = 0.73$, $\tilde{d} = -0.01$)	3.3 ± 2.1	5.1 ± 3.1
VBF $H \to \tau\tau/WW$ ($\mu = 1$, $\tilde{d} = 0$)	4.5 ± 2.9	6.9 ± 4.4
$Z \to \tau\tau$	6.6 ± 3.7	8.2 ± 3.8
Fake lepton	0.02 ± 0.20	2.3 ± 0.7
$t\bar{t}$ + single-top	3.8 ± 2.3	10.6 ± 5.5
$Z \to \ell\ell$	11 ± 18	1.8 ± 1.1
Diboson	0.70 ± 0.59	
ggF H / VH / $t\bar{t}H$, $H \to \tau\tau/WW$	0.49 ± 0.48	0.70 ± 0.30
Sum of backgrounds	23 ± 17	23.6 ± 6.1

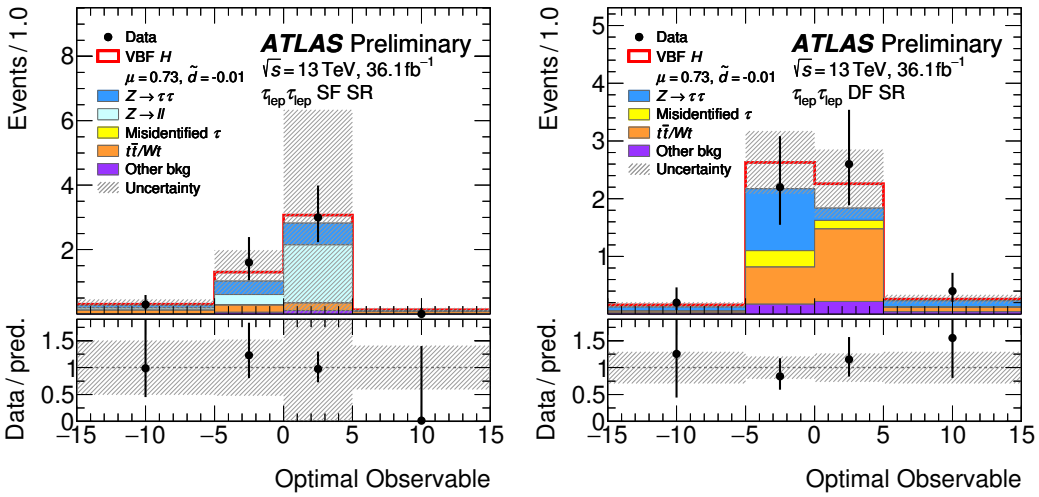

(a) (b)

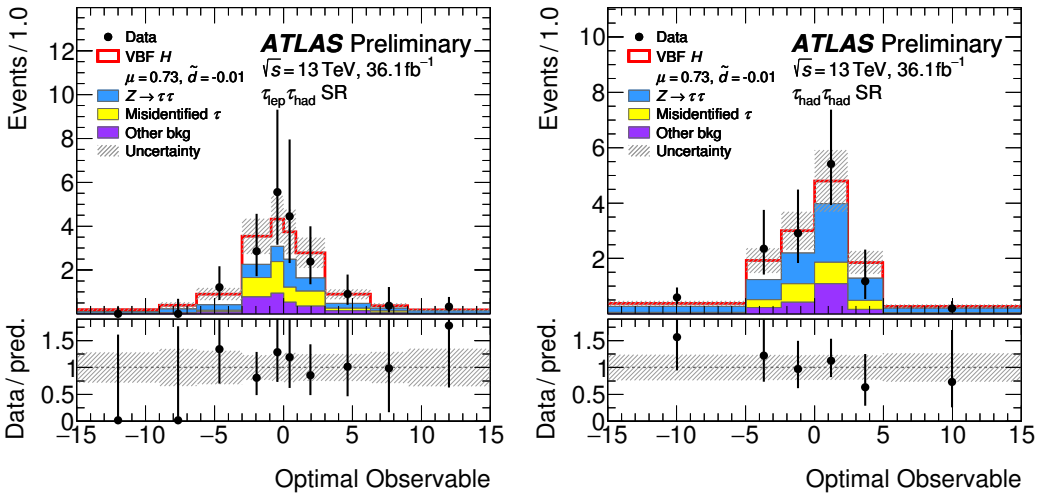

(c) (d)

Figure 5: Post-fit distributions of the event yields (divided by the bin width) as a function of the Optimal Observable in the SRs for the (a) $\tau_{\text{lep}}\tau_{\text{lep}}$ SF, (b) $\tau_{\text{lep}}\tau_{\text{lep}}$ DF, (c) $\tau_{\text{lep}}\tau_{\text{had}}$ and (d) $\tau_{\text{had}}\tau_{\text{had}}$ analysis channels. The values of $\tilde{d}$, the signal strength μ, the normalization of background processes, and nuisance parameters for the event yield prediction are set to those which minimize the NLL. The ratios of the data to the prediction are shown in the lower panels. The size of the combined statistical, experimental and theoretical uncertainties in the event yields is indicated by the hatched bands.

normalization factors based on the observed data in the background CRs in the expected ΔNLL curve result in a decrease in sensitivity to $\tilde{d}$ when compared to the pre-fit expected curve.

The effect of systematic uncertainties on the sensitivity to $\tilde{d}$ can be seen in Figure 6(b). Here, the expected ΔNLL curves are shown for $\tilde{d} = 0$ and $\mu = 1$, with and without the effect of systematic uncertainties. To assess the impact of systematic uncertainties stemming from jet reconstruction, τ lepton identification, and MC statistics, expected ΔNLL curves are also shown where the nuisance parameters corresponding to the

Table 5: Post-fit event yields in the SRs for the $\tau_{\text{lep}}\tau_{\text{had}}$ and $\tau_{\text{had}}\tau_{\text{had}}$ analysis channels. The line "Other backgrounds" includes top quark ($t\bar{t}$ and single top), diboson, and $Z \to \ell\ell$ backgrounds. Backgrounds from $W \to \tau_{\text{had}}\nu$+jets production in the $\tau_{\text{had}}\tau_{\text{had}}$ channel are also included in "Other backgrounds". For comparison, the expected signal yields for the SM expectation ($\mu = 1$, $\tilde{d} = 0$) are also shown.

Process	$\tau_{\text{lep}}\tau_{\text{had}}$	$\tau_{\text{had}}\tau_{\text{had}}$
Data	30	37
VBF $H \to \tau\tau$ ($\mu = 0.73$, $\tilde{d} = -0.01$)	11.8 ± 7.4	8.9 ± 5.6
VBF $H \to \tau\tau$ ($\mu = 1$, $\tilde{d} = 0$)	16 ± 10	12.3 ± 7.7
$Z \to \tau\tau$	7.8 ± 3.5	15.5 ± 5.2
Fake lepton/τ	6.2 ± 1.0	5.4 ± 2.7
ggF H / VH / $t\bar{t}H$, $H \to \tau\tau$	2.1 ± 1.5	2.8 ± 1.4
Other backgrounds	2.8 ± 3.1	2.3 ± 0.8
Sum of backgrounds	19.0 ± 5.5	26.0 ± 6.6

systematic uncertainties in question have been removed from the likelihood function. It is evident that the experimental uncertainties related to jet reconstruction have the largest effect on the sensitivity of this analysis to $\tilde{d}$.

To obtain insight into the preferred values of $\tilde{d}$ obtained for the individual Optimal Observable distributions in the different analysis channels, ΔNLL curves for each individual channel are shown in Figure 6(c), and compared to the combined result. For these individual ΔNLL curves, only event yield information from the other three signal regions that are not being featured is used, such that the distribution of events in the Optimal Observable in these other signal regions is not exploited in the ML-fit. For these individual channel ΔNLL curves, the signal strength is constrained to be positive, such that the ML-fit is stable and insensitive to event yield fluctuations in the individual channel SRs that arise from lower statistics. This constraint is responsible for the plateau in the ΔNLL curve occurring at negative values in the $\tau_{\text{lep}}\tau_{\text{had}}$ channel.

An observed 68% CL interval of $\tilde{d} \in [-0.090, 0.035]$ is obtained from the observed ΔNLL curve using Optimal Observable distributions in all SRs. The corresponding expected interval, based upon the expected ΔNLL curve for $\tilde{d} = 0, \mu = 1$ in Figure 6(a) is $\tilde{d} \in [-0.035, 0.033]$. This represents an improvement in the confidence interval on $\tilde{d}$ set in Ref. [34]. While no observed 95% CL interval on $\tilde{d}$ can be quoted, the corresponding expected interval is $\tilde{d} \in [-0.21, 0.15]$ at 95% CL. The asymmetry in these expected intervals stems from the slightly asymmetric Optimal Observable distribution of the background estimates in the SRs, caused by limited statistics for the background predictions.

The intervals based upon the pre-fit expected ΔNLL curve in Figure 6(a), where the nuisance parameters and background normalization factors do not take into account the observed data in the CRs, are $\tilde{d} \in [-0.032, 0.031]$ at 68% CL and $\tilde{d} \in [-0.12, 0.10]$ at 95% CL.

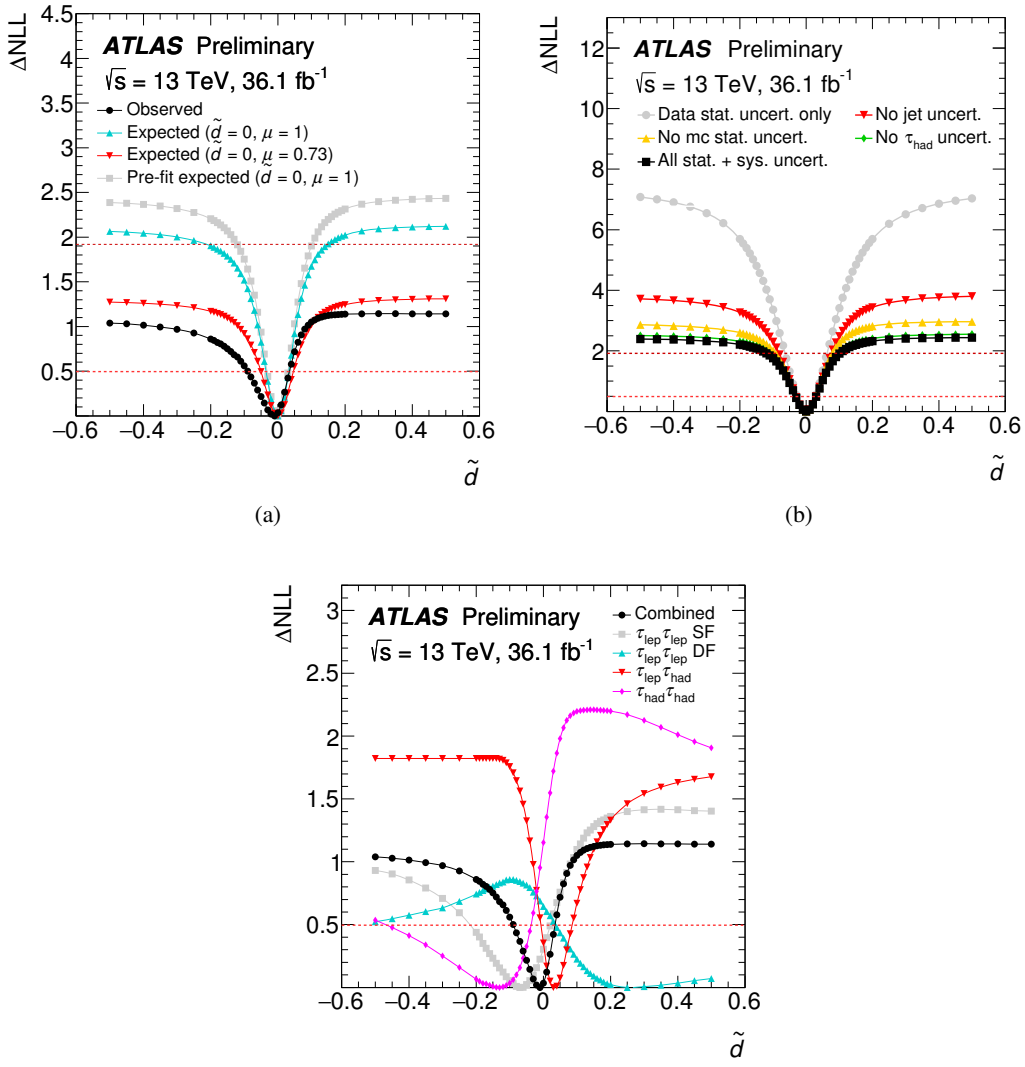

Figure 6: (a) The observed ΔNLL curve as a function of $\tilde{d}$ values. For comparison, expected ΔNLL curves are also shown. The constraints on the nuisance parameters and normalization factors are first determined in a CR-only fit, and then a fit to pseudo-data corresponding to these nuisance parameters, normalization factors, and to $\tilde{d} = 0, \mu = 1$ or $\tilde{d} = 0, \mu = 0.73$ is performed to obtain these ΔNLL curves. Moreover, a pre-fit expected ΔNLL is shown, using pseudo-data corresponding to $\tilde{d} = 0$ and $\mu = 1$ in the signal and control regions. (b) The expected ΔNLL curves comparing the sensitivity of the fit with and without systematic uncertainties. For comparison, other curves are shown which remove the effect of jet-based systematic uncertainties, τ-based systematic uncertainties, and MC statistical uncertainties. (c) The observed ΔNLL curves for each analysis channel as a function of $\tilde{d}$, compared to the combined result. For the individual analysis channel ΔNLL curves, only event yield information in the other SRs is used, ensuring that the Optimal Observable distributions in the other SRs do not influence the preferred value of $\tilde{d}$. The signal strength is constrained to be positive in these individual channel ΔNLL curves. For all figures, the dashed horizontal lines show the values of ΔNLL used to define the 68% and 95% confidence intervals.

10 Conclusion

The CP invariance of the Higgs boson coupling to vector bosons has been tested in the VBF $H \to \tau\tau$ process in 36.1 fb^{-1} of $\sqrt{s} = 13$ TeV proton–proton collision data obtained with the ATLAS detector at the LHC. For this analysis, an Optimal Observable has been utilized and confidence intervals have been set on the CP-mixing parameter $\tilde{d}$.

Since the mean of the Optimal Observable observed in data is consistent with zero, and the obtained confidence intervals on $\tilde{d}$ are consistent with the Standard Model value $\tilde{d} = 0$, no evidence of CP violation is observed in this analysis. Due to lower than expected signal yields in data, no constraints on $\tilde{d}$ can be set at 95% CL, while the corresponding Standard Model expectation is $\tilde{d} \in [-0.21, 0.15]$. An observed 68% CL interval of $\tilde{d} \in [-0.090, 0.035]$ is obtained, while the corresponding interval based on the expectation is $\tilde{d} \in [-0.035, 0.033]$.

Appendix

The modelling of the $\mathrm{BDT_{score}}$ and Optimal Observable distributions is validated in the top-quark and $Z \to \ell\ell$ CRs of the $\tau_{\mathrm{lep}}\tau_{\mathrm{lep}}$ analysis channels. Figure 7 shows the $\tau_{\mathrm{lep}}\tau_{\mathrm{lep}}$ $\mathrm{BDT_{score}}$ distributions in the top-quark CR for the $\tau_{\mathrm{lep}}\tau_{\mathrm{lep}}$ SF and DF channels, as well as in the $Z \to \ell\ell$ CR for the $\tau_{\mathrm{lep}}\tau_{\mathrm{lep}}$ SF channel. The Optimal Observable distributions are shown in Fig. 8 in the same CRs. Good modelling is observed for all these distributions.

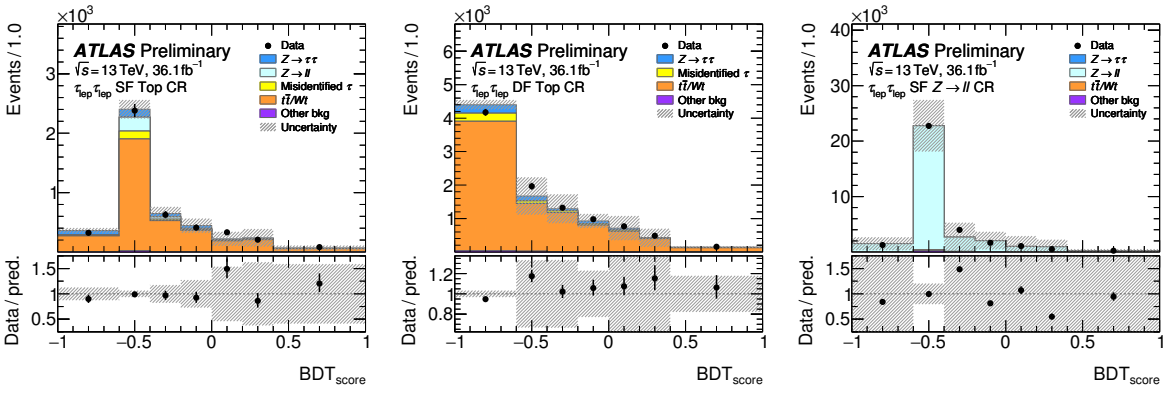

(a) (b) (c)

Figure 7: Post-fit BDT distributions in the top-quark CR for the (a) $\tau_{\mathrm{lep}}\tau_{\mathrm{lep}}$ SF and (b) $\tau_{\mathrm{lep}}\tau_{\mathrm{lep}}$ DF channels, as well as in the (c) $Z \to \ell\ell$ CR for the $\tau_{\mathrm{lep}}\tau_{\mathrm{lep}}$ SF analysis channel. The signal contamination in the CR is negligible. The size of the combined statistical, experimental, and theoretical uncertainties is indicated by the hatched bands.

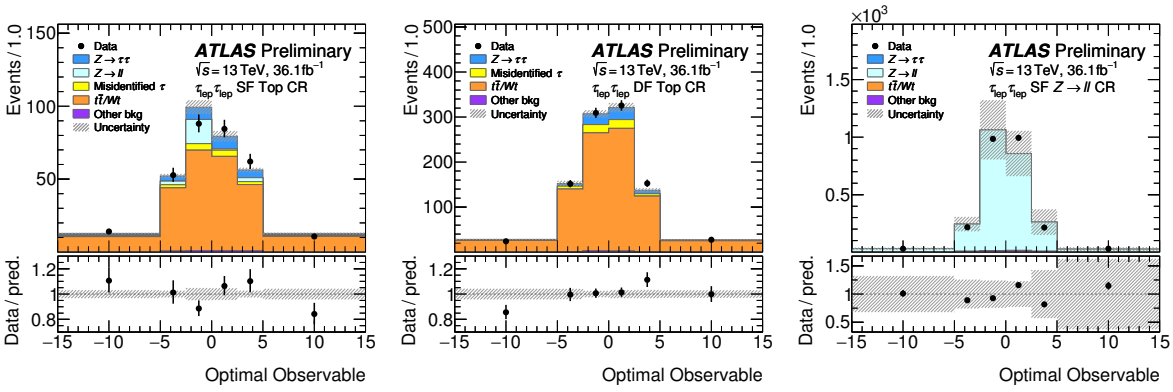

(a) (b) (c)

Figure 8: Post-fit Optimal Observable distributions in the top-quark CR for the (a) $\tau_{\mathrm{lep}}\tau_{\mathrm{lep}}$ SF and (b) $\tau_{\mathrm{lep}}\tau_{\mathrm{lep}}$ DF channels, as well as in the (c) $Z \to \ell\ell$ CR for the $\tau_{\mathrm{lep}}\tau_{\mathrm{lep}}$ SF analysis channel. The signal contamination in the CR is negligible. The size of the combined statistical, experimental, and theoretical uncertainties is indicated by the hatched bands.

References

[1] A. D. Sakharov, *Violation of CP invariance, C asymmetry, and baryon asymmetry of the universe*, Pisma Zh. Eksp. Teor. Fiz. **5** (1967) 32 (cit. on p. 2).

[2] N. Cabibbo, *Unitary Symmetry and Leptonic Decays*, Phys. Rev. Lett. **10** (1963) 531 (cit. on p. 2).

[3] M. Kobayashi and T. Maskawa, *CP Violation in the Renormalizable Theory of Weak Interaction*, Prog. Theor. Phys. **49** (1973) 652 (cit. on p. 2).

[4] J. H. Christenson, J. W. Cronin, V. L. Fitch and R. Turlay, *Evidence for the 2π Decay of the K_2^0 Meson*, Phys. Rev. Lett. **13** (1964) 138 (cit. on p. 2).

[5] KTeV Collaboration, A. Alavi-Harati et al., *Observation of Direct CP Violation in $K_{S,L} \to \pi\pi$ Decays*, Phys. Rev. Lett. **83** (1999) 22, arXiv: hep-ex/9905060 (cit. on p. 2).

[6] NA48 Collaboration, A. Lai et al., *A precise measurement of the direct CP violation parameter* $\mathrm{Re}(\varepsilon'/\varepsilon)$, Eur. Phys. J. C **22** (2001) 231, arXiv: hep-ex/0110019 (cit. on p. 2).

[7] BaBar Collaboration, B. Aubert et al., *Observation of CP Violation in the B^0 Meson System*, Phys. Rev. Lett. **87** (2001) 091801, arXiv: hep-ex/0107013 (cit. on p. 2).

[8] Belle Collaboration, K. Abe et al., *Observation of Large CP Violation in the Neutral B Meson System*, Phys. Rev. Lett. **87** (2001) 091802, arXiv: hep-ex/0107061 (cit. on p. 2).

[9] BaBar Collaboration, B. Aubert et al., *Direct CP Violating Asymmetry in $B^0 \to K^+\pi^-$ Decays*, Phys. Rev. Lett. **93** (2004) 131801, arXiv: hep-ex/0407057 (cit. on p. 2).

[10] Belle Collaboration, Y. Chao et al., *Evidence for Direct CP Violation in $B^0 \to K^+\pi^-$ Decays*, Phys. Rev. Lett. **93** (2004) 191802, arXiv: hep-ex/0408100 (cit. on p. 2).

[11] LHCb Collaboration, *First Observation of CP Violation in the Decays of B_s^0 Mesons*, Phys. Rev. Lett. **110** (2013) 221601, arXiv: 1304.6173 [hep-ex] (cit. on p. 2).

[12] LHCb Collaboration, *Observation of CP violation in $B^\pm \to DK^\pm$ decays*, Phys. Lett. B **712** (2012) 203, arXiv: 1203.3662 [hep-ex] (cit. on p. 2), Erratum: Phys. Lett. B **713** (2012) 351.

[13] LHCb Collaboration, *Observation of CP Violation in Charm Decays*, Phys. Rev. Lett. **122** (2019) 211803, arXiv: 1903.08726 [hep-ex] (cit. on p. 2).

[14] P. Huet and E. Sather, *Electroweak baryogenesis and standard model CP violation*, Phys. Rev. D **51** (1995) 379, arXiv: hep-ph/9404302 (cit. on p. 2).

[15] M. B. Gavela, P. Hernández, J. Orloff and O. Pène, *Standard model CP violation and baryon asymmetry*, Mod. Phys. Lett. A **9** (1994) 795, arXiv: hep-ph/9312215 (cit. on p. 2).

[16] A. G. Cohen, D. B. Kaplan and A. E. Nelson, *Progress in Electroweak Baryogenesis*, Ann. Rev. Nucl. Part. Sci. **43** (1993) 27, arXiv: hep-ph/9302210 (cit. on p. 2).

[17] A. Riotto and M. Trodden, *Recent Progress in Baryogenesis*, Ann. Rev. Nucl. Part. Sci. **49** (1999) 35, arXiv: hep-ph/9901362 (cit. on p. 2).

[18] W.-S. Hou, *Source of CP Violation for the Baryon Asymmetry of the Universe*, Chin. J. Phys. **47** (2009) 134, arXiv: 0803.1234 [hep-ph], URL: https://www.ps-taiwan.org/cjp/download.php?type=paper&vol=47&num=2&page=134 (cit. on p. 2).

[19] ATLAS Collaboration, *Observation of a new particle in the search for the Standard Model Higgs boson with the ATLAS detector at the LHC*, Phys. Lett. B **716** (2012) 1, arXiv: 1207.7214 [hep-ex] (cit. on p. 2).

[20] CMS Collaboration, *Observation of a new boson at a mass of 125 GeV with the CMS experiment at the LHC*, Phys. Lett. B **716** (2012) 30, arXiv: 1207.7235 [hep-ex] (cit. on p. 2).

[21] ATLAS and CMS Collaborations, *Measurements of the Higgs boson production and decay rates and constraints on its couplings from a combined ATLAS and CMS analysis of the LHC pp collision data at $\sqrt{s}$ = 7 and 8 TeV*, JHEP **08** (2016) 045, arXiv: 1606.02266 [hep-ex] (cit. on p. 2).

[22] ATLAS Collaboration, *Combined measurements of Higgs boson production and decay using up to 80 fb^{-1} of proton-proton collision data at $\sqrt{s}$ = 13 TeV collected with the ATLAS experiment*, submitted to Phys. Rev. D (2019), arXiv: 1909.02845 [hep-ex] (cit. on p. 2).

[23] CMS Collaboration, *Combined measurements of Higgs boson couplings in proton–proton collisions at $\sqrt{s}$ = 13 TeV*, Eur. Phys. J. C **79** (2019) 421, arXiv: 1809.10733 [hep-ex] (cit. on p. 2).

[24] ATLAS Collaboration, *Evidence for the spin-0 nature of the Higgs boson using ATLAS data*, Phys. Lett. B **726** (2013) 120, arXiv: 1307.1432 [hep-ex] (cit. on p. 3).

[25] ATLAS Collaboration, *Study of the spin and parity of the Higgs boson in diboson decays with the ATLAS detector*, Eur. Phys. J. C **75** (2015) 476, arXiv: 1506.05669 [hep-ex] (cit. on pp. 3, 4), Erratum: Eur. Phys. J. C **76** (2016) 152.

[26] CMS Collaboration, *Study of the Mass and Spin-Parity of the Higgs Boson Candidate via Its Decays to Z Boson Pairs*, Phys. Rev. Lett. **110** (2013) 081803, arXiv: 1212.6639 [hep-ex] (cit. on p. 3).

[27] ATLAS Collaboration, *Measurements of Higgs boson properties in the diphoton decay channel with 36 fb^{-1} of pp collision data at $\sqrt{s}$ = 13 TeV with the ATLAS detector*, Phys. Rev. D **98** (2018) 052005, arXiv: 1802.04146 [hep-ex] (cit. on p. 3).

[28] ATLAS Collaboration, *Measurement of the Higgs boson coupling properties in the $H \to ZZ^* \to 4\ell$ decay channel at $\sqrt{s}$ = 13 TeV with the ATLAS detector*, JHEP **03** (2018) 095, arXiv: 1712.02304 [hep-ex] (cit. on p. 3).

[29] CMS Collaboration, *Combined search for anomalous pseudoscalar HVV couplings in $VH(H \to b\bar{b})$ production and $H \to VV$ decay*, Phys. Lett. B **759** (2016) 672, arXiv: 1602.04305 [hep-ex] (cit. on p. 3).

[30] CMS Collaboration, *Constraints on the spin-parity and anomalous HVV couplings of the Higgs boson in proton collisions at 7 and 8 TeV*, Phys. Rev. D **92** (2015) 012004, arXiv: 1411.3441 [hep-ex] (cit. on p. 3).

[31] CMS Collaboration, *Constraints on anomalous Higgs boson couplings using production and decay information in the four-lepton final state*, Phys. Lett. B **775** (2017) 1, arXiv: 1707.00541 [hep-ex] (cit. on p. 3).

[32] CMS Collaboration, *Measurements of the Higgs boson width and anomalous HVV couplings from on-shell and off-shell production in the four-lepton final state*, Phys. Rev. D **99** (2019) 112003, arXiv: 1901.00174 [hep-ex] (cit. on p. 3).

[33] CMS Collaboration, *Constraints on anomalous HVV couplings from the production of Higgs bosons decaying to τ lepton pairs*, submitted to Phys. Rev. D (2019), arXiv: 1903.06973 [hep-ex] (cit. on p. 3).

[34] ATLAS Collaboration, *Test of CP invariance in vector-boson fusion production of the Higgs boson using the Optimal Observable method in the ditau decay channel with the ATLAS detector*, Eur. Phys. J. C **76** (2016) 658, arXiv: 1602.04516 [hep-ex] (cit. on pp. 3, 4, 6, 7, 18).

[35] D. Atwood and A. Soni, *Analysis for magnetic moment and electric dipole moment, form-factors of the top quark via $e^+e^- \to t\bar{t}$*, Phys. Rev. D **45** (1992) 2405 (cit. on p. 3).

[36] M. Davier, L. Duflot, F. Le Diberder and A. Rouge, *The optimal method for the measurement of tau polarization*, Phys. Lett. B **306** (1993) 411 (cit. on p. 3).

[37] M. Diehl and O. Nachtmann, *Optimal observables for the measurement of three gauge boson couplings in $e^+e^- \to W^+W^-$*, Z. Phys. C **62** (1994) 397 (cit. on p. 3).

[38] J. Brehmer, F. Kling, T. Plehn and T. M. P. Tait, *Better Higgs-CP tests through information geometry*, Phys. Rev. D **97** (2018) 095017, arXiv: 1712.02350 [hep-ph] (cit. on pp. 3–5).

[39] ATLAS Collaboration, *Cross-section measurements of the Higgs boson decaying into a pair of τ-leptons in proton–proton collisions at $\sqrt{s} = 13$ TeV with the ATLAS detector*, Phys. Rev. D **99** (2019) 072001, arXiv: 1811.08856 [hep-ex] (cit. on pp. 3, 7, 8, 11, 13).

[40] L3 Collaboration, P. Achard et al., *Search for anomalous couplings in the Higgs sector at LEP*, Phys. Lett. B **589** (2004) 89, arXiv: hep-ex/0403037 (cit. on p. 4).

[41] W. Buchmuller and D. Wyler, *Effective lagrangian analysis of new interactions and flavor conservation*, Nucl. Phys. B **268** (1986) 621 (cit. on p. 4).

[42] V. Hankele, G. Klämke, D. Zeppenfeld and T. Figy, *Anomalous Higgs boson couplings in vector boson fusion at the CERN LHC*, Phys. Rev. D **74** (2006) 095001, arXiv: hep-ph/0609075 (cit. on pp. 4, 6).

[43] M. Ciccolini, A. Denner and S. Dittmaier, *Strong and Electroweak Corrections to the Production of a Higgs Boson + 2 Jets via Weak Interactions at the Large Hadron Collider*, Phys. Rev. Lett. **99** (2007) 161803, arXiv: 0707.0381 [hep-ph] (cit. on pp. 5, 7).

[44] M. Ciccolini, A. Denner and S. Dittmaier, *Electroweak and QCD corrections to Higgs production via vector-boson fusion at the LHC*, Phys. Rev. D **77** (2008) 013002, arXiv: 0710.4749 [hep-ph] (cit. on pp. 5, 7).

[45] A. Denner, S. Dittmaier, S. Kallweit and A. Mück, *HAWK 2.0: A Monte Carlo program for Higgs production in vector-boson fusion and Higgs strahlung at hadron colliders*, Comput. Phys. Commun. **195** (2015) 161, arXiv: 1412.5390 [hep-ph] (cit. on p. 5).

[46] H.-L. Lai et al., *New parton distributions for collider physics*, Phys. Rev. D **82** (2010) 074024, arXiv: 1007.2241 [hep-ph] (cit. on pp. 6, 7).

[47] ATLAS Collaboration, *The ATLAS Experiment at the CERN Large Hadron Collider*, JINST **3** (2008) S08003 (cit. on p. 6).

[48] ATLAS Collaboration, *ATLAS Insertable B-Layer Technical Design Report*, ATLAS-TDR-19, 2010, URL: https://cds.cern.ch/record/1291633, *ATLAS Insertable B-Layer Technical Design Report Addendum*, ATLAS-TDR-19-ADD-1, 2012, URL: https://cds.cern.ch/record/1451888 (cit. on p. 6).

[49] B. Abbott et al., *Production and integration of the ATLAS Insertable B-Layer*, JINST **13** (2018) T05008, arXiv: 1803.00844 [physics.ins-det] (cit. on p. 6).

[50] T. Gleisberg et al., *Event generation with SHERPA 1.1*, JHEP **02** (2009) 007, arXiv: 0811.4622 [hep-ph] (cit. on p. 7).

[51] T. Gleisberg and S. Höche, *Comix, a new matrix element generator*, JHEP **12** (2008) 039, arXiv: 0808.3674 [hep-ph] (cit. on p. 7).

[52] F. Cascioli, P. Maierhöfer and S. Pozzorini, *Scattering Amplitudes with Open Loops*, Phys. Rev. Lett. **108** (2012) 111601, arXiv: 1111.5206 [hep-ph] (cit. on p. 7).

[53] S. Höche, F. Krauss, S. Schumann and F. Siegert, *QCD matrix elements and truncated showers*, JHEP **05** (2009) 053, arXiv: 0903.1219 [hep-ph] (cit. on p. 7).

[54] ATLAS Collaboration, *Measurement of the cross-section for electroweak production of dijets in association with a Z boson in pp collisions at* $\sqrt{s} = 13$ *TeV with the ATLAS detector*, Phys. Lett. B **775** (2017) 206, arXiv: 1709.10264 [hep-ex] (cit. on p. 7).

[55] P. Nason, *A new method for combining NLO QCD with shower Monte Carlo algorithms*, JHEP **11** (2004) 040, arXiv: hep-ph/0409146 (cit. on p. 7).

[56] S. Frixione, P. Nason and C. Oleari, *Matching NLO QCD computations with parton shower simulations: the POWHEG method*, JHEP **11** (2007) 070, arXiv: 0709.2092 [hep-ph] (cit. on p. 7).

[57] S. Alioli, P. Nason, C. Oleari and E. Re, *A general framework for implementing NLO calculations in shower Monte Carlo programs: the POWHEG BOX*, JHEP **06** (2010) 043, arXiv: 1002.2581 [hep-ph] (cit. on p. 7).

[58] K. Hamilton, P. Nason and G. Zanderighi, *MINLO: multi-scale improved NLO*, JHEP **10** (2012) 155, arXiv: 1206.3572 [hep-ph] (cit. on p. 7).

[59] P. Nason and C. Oleari, *NLO Higgs boson production via vector-boson fusion matched with shower in POWHEG*, JHEP **02** (2010) 037, arXiv: 0911.5299 [hep-ph] (cit. on p. 7).

[60] J. Butterworth et al., *PDF4LHC recommendations for LHC Run II*, J. Phys. G **43** (2016) 023001, arXiv: 1510.03865 [hep-ph] (cit. on p. 7).

[61] T. Sjöstrand et al., *An introduction to PYTHIA 8.2*, Comput. Phys. Commun. **191** (2015) 159, arXiv: 1410.3012 [hep-ph] (cit. on p. 7).

[62] P. Bolzoni, F. Maltoni, S.-O. Moch and M. Zaro, *Higgs Boson Production via Vector-Boson Fusion at Next-to-Next-to-Leading Order in QCD*, Phys. Rev. Lett. **105** (2010) 011801, arXiv: 1003.4451 [hep-ph] (cit. on p. 7).

[63] M. Bahr et al., *Herwig++ physics and manual*, Eur. Phys. J. C **58** (2008) 639, arXiv: 0803.0883 [hep-ph] (cit. on p. 7).

[64] J. Bellm et al., *Herwig 7.0/Herwig++ 3.0 release note*, Eur. Phys. J. C **76** (2016) 196, arXiv: 1512.01178 [hep-ph] (cit. on p. 7).

[65] C. Anastasiou, C. Duhr, F. Dulat, F. Herzog and B. Mistlberger, *Higgs Boson Gluon-Fusion Production in QCD at Three Loops*, Phys. Rev. Lett. **114** (2015) 212001, arXiv: 1503.06056 [hep-ph] (cit. on p. 7).

[66] C. Anastasiou et al., *High precision determination of the gluon fusion Higgs boson cross-section at the LHC*, JHEP **05** (2016) 058, arXiv: 1602.00695 [hep-ph] (cit. on p. 7).

[67] S. Actis, G. Passarino, C. Sturm and S. Uccirati, *NLO electroweak corrections to Higgs boson production at hadron colliders*, Phys. Lett. B **670** (2008) 12, arXiv: 0809.1301 [hep-ph] (cit. on p. 7).

[68] C. Anastasiou, R. Boughezal and F. Petriello, *Mixed QCD-electroweak corrections to Higgs boson production in gluon fusion*, JHEP **04** (2009) 003, arXiv: 0811.3458 [hep-ph] (cit. on p. 7).

[69] J. M. Campbell et al., *NLO Higgs boson production plus one and two jets using the POWHEG BOX, MadGraph4 and MCFM*, JHEP **07** (2012) 092, arXiv: 1202.5475 [hep-ph] (cit. on p. 7).

[70] K. Hamilton, P. Nason, E. Re and G. Zanderighi, *NNLOPS simulation of Higgs boson production*, JHEP **10** (2013) 222, arXiv: 1309.0017 [hep-ph] (cit. on p. 7).

[71] K. Hamilton, P. Nason and G. Zanderighi, *Finite quark-mass effects in the NNLOPS POWHEG+MiNLO Higgs generator*, JHEP **05** (2015) 140, arXiv: 1501.04637 [hep-ph] (cit. on p. 7).

[72] G. Luisoni, P. Nason, C. Oleari and F. Tramontano, *$HW^{\pm}$/HZ + 0 and 1 jet at NLO with the POWHEG BOX interfaced to GoSam and their merging within MiNLO*, JHEP **10** (2013) 083, arXiv: 1306.2542 [hep-ph] (cit. on p. 7).

[73] O. Brein, A. Djouadi and R. Harlander, *NNLO QCD corrections to the Higgs-strahlung processes at hadron colliders*, Phys. Lett. B **579** (2004) 149, arXiv: hep-ph/0307206 (cit. on p. 7).

[74] A. Denner, S. Dittmaier, S. Kallweit and A. Mück, *Electroweak corrections to Higgs-strahlung off W/Z bosons at the Tevatron and the LHC with Hawk*, JHEP **03** (2012) 075, arXiv: 1112.5142 [hep-ph] (cit. on p. 7).

[75] L. Altenkamp, S. Dittmaier, R. V. Harlander, H. Rzehak and T. J. E. Zirke, *Gluon-induced Higgs-strahlung at next-to-leading order QCD*, JHEP **02** (2013) 078, arXiv: 1211.5015 [hep-ph] (cit. on p. 7).

[76] R. V. Harlander, A. Kulesza, V. Theeuwes and T. Zirke, *Soft gluon resummation for gluon-induced Higgs Strahlung*, JHEP **11** (2014) 082, arXiv: 1410.0217 [hep-ph] (cit. on p. 7).

[77] J. Alwall et al., *The automated computation of tree-level and next-to-leading order differential cross sections, and their matching to parton shower simulations*, JHEP **07** (2014) 079, arXiv: 1405.0301 [hep-ph] (cit. on p. 7).

[78] R. Frederix and S. Frixione, *Merging meets matching in MC@NLO*, JHEP **12** (2012) 061, arXiv: 1209.6215 [hep-ph] (cit. on p. 7).

[79] R. D. Ball et al., *Parton distributions for the LHC Run II*, JHEP **04** (2015) 040, arXiv: 1410.8849 [hep-ph] (cit. on p. 7).

[80] W. Beenakker et al., *Higgs Radiation Off Top Quarks at the Tevatron and the LHC*, Phys. Rev. Lett. **87** (2001) 201805, arXiv: hep-ph/0107081 (cit. on p. 7).

[81] W. Beenakker et al., *NLO QCD corrections to $t\bar{t}H$ production in hadron collisions*, Nucl. Phys. B **653** (2003) 151, arXiv: hep-ph/0211352 (cit. on p. 7).

[82] S. Dawson, L. Orr, L. Reina and D. Wackeroth, *Next-to-leading order QCD corrections to $pp \to t\bar{t}h$ at the CERN Large Hadron Collider*, Phys. Rev. D **67** (2003) 071503, arXiv: hep-ph/0211438 (cit. on p. 7).

[83] S. Dawson, C. Jackson, L. Orr, L. Reina and D. Wackeroth, *Associated Higgs boson production with top quarks at the CERN Large Hadron Collider: NLO QCD corrections*, Phys. Rev. D **68** (2003) 034022, arXiv: hep-ph/0305087 (cit. on p. 7).

[84] Y. Zhang, W.-G. Ma, R.-Y. Zhang, C. Chen and L. Guo, *QCD NLO and EW NLO corrections to $t\bar{t}H$ production with top quark decays at hadron collider*, Phys. Lett. B **738** (2014) 1, arXiv: 1407.1110 [hep-ph] (cit. on p. 7).

[85] S. Frixione, V. Hirschi, D. Pagani, H.-S. Shao and M. Zaro, *Electroweak and QCD corrections to top-pair hadroproduction in association with heavy bosons*, JHEP **06** (2015) 184, arXiv: 1504.03446 [hep-ph] (cit. on p. 7).

[86] S. Höche, F. Krauss, M. Schönherr and F. Siegert, *QCD matrix elements + parton showers. The NLO case*, JHEP **04** (2013) 027, arXiv: 1207.5030 [hep-ph] (cit. on p. 7).

[87] S. Schumann and F. Krauss, *A parton shower algorithm based on Catani–Seymour dipole factorisation*, JHEP **03** (2008) 038, arXiv: 0709.1027 [hep-ph] (cit. on p. 7).

[88] K. Melnikov and F. Petriello, *Electroweak gauge boson production at hadron colliders through $O(\alpha_s^2)$*, Phys. Rev. D **74** (2006) 114017, arXiv: hep-ph/0609070 (cit. on p. 7).

[89] C. Anastasiou, L. Dixon, K. Melnikov and F. Petriello, *High precision QCD at hadron colliders: Electroweak gauge boson rapidity distributions at next-to-next-to leading order*, Phys. Rev. D **69** (2004) 094008, arXiv: hep-ph/0312266 (cit. on p. 7).

[90] S. Alioli, S.-O. Moch and P. Uwer, *Hadronic top-quark pair-production with one jet and parton showering*, JHEP **01** (2012) 137, arXiv: 1110.5251 [hep-ph] (cit. on p. 7).

[91] T. Sjöstrand, S. Mrenna and P. Z. Skands, *PYTHIA 6.4 Physics and Manual*, JHEP **05** (2006) 026, arXiv: hep-ph/0603175 (cit. on p. 7).

[92] M. Czakon, P. Fiedler and A. Mitov, *Total Top-Quark Pair-Production Cross Section at Hadron Colliders Through $O(\alpha_S^4)$*, Phys. Rev. Lett. **110** (2013) 252004, arXiv: 1303.6254 [hep-ph] (cit. on p. 7).

[93] E. Re, *Single-top Wt-channel production matched with parton showers using the POWHEG method*, Eur. Phys. J. C **71** (2011) 1547, arXiv: 1009.2450 [hep-ph] (cit. on p. 7).

[94] F. Maltoni, K. Mawatari and M. Zaro, *Higgs characterisation via vector-boson fusion and associated production: NLO and parton-shower effects*, Eur. Phys. J. C **74** (2014) 2710, arXiv: 1311.1829 [hep-ph] (cit. on p. 7).

[95] ATLAS Collaboration, *The ATLAS Simulation Infrastructure*, Eur. Phys. J. C **70** (2010) 823, arXiv: 1005.4568 [physics.ins-det] (cit. on p. 7).

[96] S. Agostinelli et al., *GEANT4—a simulation toolkit*, Nucl. Instrum. Meth. A **506** (2003) 250 (cit. on p. 7).

[97] A. D. Martin, W. J. Stirling, R. S. Thorne and G. Watt, *Parton distributions for the LHC*, Eur. Phys. J. **C63** (2009) 189, arXiv: 0901.0002 [hep-ph] (cit. on p. 7).

[98] ATLAS Collaboration, *Summary of ATLAS Pythia 8 tunes*, ATL-PHYS-PUB-2012-003, 2012, URL: https://cds.cern.ch/record/1474107 (cit. on p. 7).

[99] J. H. Friedman, *Greedy function approximation: A gradient boosting machine.*, Ann. Statist. **29** (2001) 1189 (cit. on p. 8).

[100] R. K. Ellis, I. Hinchliffe, M. Soldate and J. J. van der Bij, *Higgs decay to $\tau^+\tau^-$: A possible signature of intermediate mass Higgs bosons at high energy hadron colliders*, Nucl. Phys. **B297** (1988) 221 (cit. on p. 9).

[101] ATLAS Collaboration, *Observation and measurement of Higgs boson decays to WW^* with the ATLAS detector*, Phys. Rev. D **92** (2015) 012006, arXiv: 1412.2641 [hep-ex] (cit. on p. 9).

[102] ATLAS Collaboration, *Performance of b-jet identification in the ATLAS experiment*, JINST **11** (2016) P04008, arXiv: 1512.01094 [hep-ex] (cit. on pp. 9, 13).

[103] ATLAS Collaboration, *Optimisation of the ATLAS b-tagging performance for the 2016 LHC Run*, ATL-PHYS-PUB-2016-012, 2016, URL: https://cds.cern.ch/record/2160731 (cit. on pp. 9, 13).

[104] A. Elagin, P. Murat, A. Pranko and A. Safonov, *A new mass reconstruction technique for resonances decaying to $\tau\tau$*, Nucl. Instrum. Meth. A **654** (2011) 481, arXiv: 1012.4686 [hep-ex] (cit. on p. 9).

[105] ATLAS Collaboration, *Jet Calibration and Systematic Uncertainties for Jets Reconstructed in the ATLAS Detector at $\sqrt{s}$ = 13 TeV*, ATL-PHYS-PUB-2015-015, 2015, URL: https://cds.cern.ch/record/2037613 (cit. on p. 13).

[106] ATLAS Collaboration, *Jet energy scale measurements and their systematic uncertainties in proton–proton collisions at $\sqrt{s}$ = 13 TeV with the ATLAS detector*, Phys. Rev. D **96** (2017) 072002, arXiv: 1703.09665 [hep-ex] (cit. on p. 13).

[107] ATLAS Collaboration, *Reconstruction, Energy Calibration, and Identification of Hadronically Decaying Tau Leptons in the ATLAS Experiment for Run-2 of the LHC*, ATL-PHYS-PUB-2015-045, 2015, URL: https://cds.cern.ch/record/2064383 (cit. on p. 13).

[108] ATLAS Collaboration, *Measurement of the tau lepton reconstruction and identification performance in the ATLAS experiment using pp collisions at $\sqrt{s}$ = 13 TeV*, ATLAS-CONF-2017-029, 2017, URL: https://cds.cern.ch/record/2261772 (cit. on p. 13).

[109] ATLAS Collaboration, *Electron and photon energy calibration with the ATLAS detector using 2015–2016 LHC proton–proton collision data*, JINST **14** (2019) P03017, arXiv: 1812.03848 [hep-ex] (cit. on p. 13).

[110] ATLAS Collaboration, *Electron reconstruction and identification in the ATLAS experiment using the 2015 and 2016 LHC proton–proton collision data at $\sqrt{s}$ = 13 TeV*, Eur. Phys. J. C **79** (2019) 639, arXiv: 1902.04655 [hep-ex] (cit. on p. 13).

[111] ATLAS Collaboration, *Muon reconstruction performance of the ATLAS detector in proton–proton collision data at $\sqrt{s}$ = 13 TeV*, Eur. Phys. J. C **76** (2016) 292, arXiv: 1603.05598 [hep-ex] (cit. on p. 13).

[112] ATLAS Collaboration, *Performance of missing transverse momentum reconstruction with the ATLAS detector using proton–proton collisions at $\sqrt{s}$ = 13 TeV*, Eur. Phys. J. C **78** (2018) 903, arXiv: 1802.08168 [hep-ex] (cit. on p. 13).

[113] ATLAS Collaboration, *Luminosity determination in pp collisions at $\sqrt{s}$ = 13 TeV using the ATLAS detector at the LHC*, ATLAS-CONF-2019-021, 2019, URL: https://cds.cern.ch/record/2677054 (cit. on p. 13).

[114] LHC Higgs Cross Section Working Group, *Handbook of LHC Higgs Cross Sections: 4. Deciphering the Nature of the Higgs Sector*, (2016), arXiv: 1610.07922 [hep-ph] (cit. on p. 13).